

GAS EMISSION FROM DEBRIS DISKS AROUND A AND F STARS

KYRYL ZAGOROVSKY

IBBME, University of Toronto, Toronto, ON M5S 3G9, Canada

ALEXIS BRANDEKER

Department of Astronomy, Stockholm University, SE-106 91 Stockholm, Sweden

YANQIN WU

Department of Astronomy and Astrophysics, University of Toronto, Toronto, ON M5S 3H4, Canada

Draft version October 11, 2018

ABSTRACT

Gas has been detected in a number of debris disk systems. This gas may have arisen from grain sublimation or grain photodesorption. It interacts with the surrounding dust grains through a number of charge and heat exchanges. Studying the chemical composition and physical state of this gas can therefore reveal much about the dust component in these debris disks. We have produced a new code, ONTARIO, to address gas emission from dusty gas-poor disks around A–F stars. This code computes the gas ionization and thermal balance self-consistently, with particular care taken of heating/cooling mechanisms. Line emission spectra are then produced for each species (up to zinc) by statistical equilibrium calculations of the atomic/ionic energy levels. For parameters that resemble the observed β Pictoris gas disk, we find that the gas is primarily heated by photoelectric emission from dust grains, and primarily cooled through the C II 157.7 μm line emission. The gas can be heated to a temperature that is warmer than that of the dust and may in some cases reach temperature for thermal escape. The dominant cooling line, C II 157.7 μm , should be detectable by *Herschel*, while the O I 63.2 μm line will be too faint. We also study the dependence of the cooling line fluxes on a variety of disk parameters, in light of the much improved sensitivity to thermal line emission in the mid/far infrared and at sub-millimeter wavelengths provided by, in particular, *Herschel*, *SOFIA*, and *ALMA*. These new instruments will yield much new information about dusty debris disks.

Subject headings: Stars: Circumstellar Matter, Stars: Planetary Systems: Formation, Stars: Planetary Systems: Protoplanetary Disks, Scattering, Stars: Individual: Constellation Name: β Pictoris

1. INTRODUCTION

During the T Tauri phase, models have shown that giant planet formation rely heavily on the timescale and manner in which gas disks disperse (see, e.g. Ida & Lin 2004). We now know that some of this gas is incorporated into gaseous giant planets, while some is lost to the stars, and that most of the gas disappears on timescales of a few Myr (e.g. Zuckerman et al. 1995; Haisch et al. 2001; Jayawardhana et al. 2006; Pascucci et al. 2006). However, we still do not know whether most of the gas disks around T Tauri stars is photoevaporated by the star (see, e.g. Gorti & Hollenbach 2009), blown away by wind (Lovelace et al. 2008), or accreted onto the star due to viscous diffusion (Lynden-Bell & Pringle 1974). Which mechanism dominates will determine how long gas resides in different parts of the disk. Observing protoplanetary disks near their final stages may yield clue to this puzzle.

Debris disks are circumstellar disks that show emission from dust. These disks are detectable for up to a few Gyr (Holland et al. 1998; Spangler et al. 2001; Rieke et al. 2005). Both the level of emission and the

fraction of stars with a detectable excess decay with time and can be interpreted, at least for the case of A stars, as steady state collisional processing of planetesimals formed during the proto-planetary disk phase (Dominik & Decin 2003; Wyatt et al. 2007). There is some evidence that gas may persist in debris disks for an extended period of time, at least in some systems. For example, atomic gas in Keplerian rotation has been detected around the ~ 12 Myr old main-sequence star β Pic (Hobbs et al. 1985; Brandeker et al. 2004). Gas has also been found around post-T Tauri stars (e.g. Redfield et al. 2007), and even stars as old as 200 Myr (e.g. σ Her; Chen & Jura 2003). However, it is not clear whether this gas is primordial (left-over proto-planetary material) or secondary, generated by, e.g., sublimation of planetesimals (Beust & Valiron 2007), vaporization of colliding planetesimals (Czechowski & Mann 2007), and/or photo-desorption of dust (Chen et al. 2007). If gas is indeed secondary (as dynamical arguments suggest, see Fernández, Brandeker, & Wu 2006), it presents an exciting new tool to study the compositions of solid bodies in extra-solar systems, inaccessible otherwise. In addition, even a small quantity of gas may also significantly affect the dynamics of the dust and cause grain concentrations, mimicking the bright rings seen in young debris disks like HR 4796A (Klahr & Lin 2005; Besla & Wu 2007). Fur-

thermore, gas present during late stages of planet formation could damp eccentricities of the planetesimals enough to reduce their relative speed, thereby aiding the build up of rocky planets.

Unfortunately, the information currently available on the manner in which gas disperses in circumstellar disks is scarce, owing to the great difficulty in detecting gas in these environments. Accretion traces only the sub-AU region of the disk, leaving the outer gas disk largely unconstrained. Molecular emission from CO in young circumstellar disks has been detected in the near-infrared (NIR) and in the mm (e.g. Najita et al. 2003). The NIR emission is limited to hot CO (~ 1000 K), while the detection of mm emission from cold CO is hampered by limited sensitivity due to beam dilution (e.g. Pascucci et al. 2006). Direct detection of H₂ in the ultra violet (UV) and NIR is also made possible by either very hot or fluorescent gas (pumped by Ly α , Herczeg et al. 2006). The rotational lines H₂ S(0) and S(1) emitted from colder gas ($\lesssim 100$ K) are unfortunately weak and difficult to observe: a Spitzer IRS survey of young stars that are expected to have gas disks yielded only upper limits on the gas disk mass (upper limits $\gtrsim 100 M_{\oplus}$, Chen et al. 2006). An alternative is to observe stellar light scattered resonantly by the gas, but this requires a spatially resolved disk to be detectable. To date, only the disk around β Pic has been detected in such a way (Olofsson et al. 2001; Brandeker et al. 2004). Should the disk be oriented edge-on, the circumstellar gas can also be observed in absorption (e.g., Redfield 2007; Roberge & Weinberger 2008).

Here, we study infrared atomic cooling lines as promising agents for characterizing gas in tenuous disks, including late stage protoplanetary disks and debris disks. Three of the most abundant species, oxygen, carbon, and silicon, all have ground-state fine transitions at infrared wavelengths that act as effective coolants. Oxygen, in the low-density environment of these disks, is likely to be in the atomic form: the molecular repositories for oxygen (H₂O, OH, and CO; e.g. Kamp & Bertoldi 2000) are dissociated easily in the circumstellar environment, while the ionization potential for oxygen is sufficiently high for it to remain neutral. Moreover, neutral oxygen does not have strong resonant transitions in the optical and UV, and is thus not easily removed by radiation pressure, unlike some other species (Fernández et al. 2006). Of all thermally excited cooling lines, the O I 63 μ m line is expected to be the brightest for a large range of disk masses in late-type stars (G–K; Gorti & Hollenbach 2004). However, in optically thin disks around early-type stars (F or earlier), carbon is expected to be significantly ionized (Fernández et al. 2006), boosting the C II 158 μ m cooling line. Finally, if cooling by the O I and C II lines saturates (i.e. the line fluxes no longer rise with temperature due to the saturated occupation of the excited level, see eq. [8]), Si II-cooling may become important.

The O I 63 μ m and C II 158 μ m lines both lie within the spectral range of the far-infrared to sub-millimeter *Herschel* space telescope, scheduled to start science operations in early 2010. The telescope has a passively cooled 3.5 m mirror and three instruments PACS, SPIRE, and HIFI that together cover the 55–672 μ m with both imaging and spectroscopy capabilities. As such, *Herschel* is well positioned to investigate the tenuous circumstellar

disks we are discussing here and partly motivated this study.

Predicting the expected luminosity of gas and interpreting potential detections require detailed modeling of the physical circumstances, such as the radiation field from the star, the spatial distribution and content of the gas and dust, etc. Debris disks are known to be dusty with little gas, meaning that the set of assumptions and approximations that can be used are different from other environments, such as the interstellar medium where well-tested codes exist (e.g. CLOUDY, Ferland 2005). Debris disks are generally optically thin, which simplifies the radiative transfer and enables modeling of more general three-dimensional distributions with less computational resources. On the other hand, a more detailed treatment is required for the thermal balance, as fluorescence is generally important due to the strong radiation field from the star in combination with low gas densities. This implies computing the statistical equilibrium (SE) for a large number of energy levels in cooling species.

We have developed a numerical model ONTARIO (“optically thin thermal and ionization equilibrium code”) to investigate the importance of O I 63 μ m and C II 158 μ m fine-structure cooling lines as tracers for gas in dusty but optically thin disks around early-type (A–F) stars. This is intended to complement similar analysis made for later-type stars (G–K) by Gorti & Hollenbach (2004). The code takes stellar flux, gas and dust profiles as input parameters and performs self-consistent computation of ionization and thermal balance (§ 2) in the disk. Once elemental ionizations and gas temperature have been determined, a full SE computation is performed for a number of atomic species to identify the dominant emission and absorption lines.

To test the code, we use the well-studied β Pictoris disk as a benchmark case in § 3, and compare the numerical model with observed gas disk properties. In § 4.1, we keep stellar parameters at their β Pic values but replace the gas and dust distributions with more simplified Gaussian profiles, and take this configuration as the fiducial debris disk. Fiducial case temperature and ionization profiles are analyzed in § 4.1.1 and § 4.1.3. We also compute integrated luminosities for the main fine-structure cooling lines (§ 4.1.2) and identify the dominant emission and absorption lines (§ 4.1.4). In § 4.2 we investigate the dependence of emitted line luminosities on the model parameters, in particular how they scale with disk gas, geometry, mass and composition, and the spectral type of the central star. Conclusions are drawn in § 5.

Throughout the paper, we adopt the cgs units except where noted.

2. THERMAL PROCESSES MODELED IN ONTARIO

The ONTARIO model was designed to simulate gas in dusty disks around early-type stars. The code self-consistently computes the thermal and ionization states of the gas in this environment. All gas is assumed to be present in atomic or ionized form: the hard radiation fields surrounding these early-type stars rapidly photo-dissociate molecules into individual atoms or ions (Kamp et al. 2003; Jonkheid et al. 2006); thus no chemistry computation is included. Ionizations for atomic elements from hydrogen to zinc are considered, up to the second ionization state. The model assumes both dust

and gas to be optically thin, so no complex radiative transfer calculations are performed. This makes the code effectively zero-dimensional as each bin is treated independently of all others, greatly increasing computational performance. Details of the code, including how ionization and statistical equilibrium is treated, is presented in the Appendix. Here, we discuss the main processes that enter the thermal balance.

A number of heating and cooling mechanisms that determine the gas temperature in debris disks have been investigated by Kamp & van Zadelhoff (2001, hereafter KvZ01) and Besla & Wu (2007, hereafter BW07). Observed upper limits on the gas content of debris disks (Thi et al. 2001; Chen & Jura 2003; Roberge et al. 2005) and theoretical inferences (Fernández et al. 2006) suggest that gas in debris disk is non-primordial and is depleted in hydrogen. Furthermore, even when assuming solar abundance of hydrogen, it was shown by BW07 that heating arising from H₂ collisional de-excitation, photodissociation and formation on dust, as well as cooling from H₂ ro-vibrational lines, are negligible when compared to the photoelectric heating by grains. For these reasons, we do not include H₂-dependent heating and cooling processes. We do include, however, the atomic hydrogen contribution to cooling via Ly α emission at very high temperatures ($T > 5000$ K). Also excluded from computation are coolings by vibrational/rotational transitions of molecular CO and CH. These molecular species may arise from evaporating cometary bodies. However, they are believed to be quickly photodissociated around the early-type stars that are the target of this study (Kamp et al. 2003). Indeed, *HST* UV observations of β Pic failed to detect significant amounts of CO in the system (Roberge et al. 2000).

The gas temperature is solved at every spatial grid assuming that heating and cooling processes balance each other locally.

2.1. Heating

Relevant heating processes include: photoelectric heating by dust (PE), photoionization of gas by the stellar light (PI), and gas-grain collisions (GG). The last one becomes a cooling mechanism for the gas when $T_{\text{gas}} > T_{\text{dust}}$. For β Pic-like disks, BW07 have shown that photoelectric (PE) heating is by far the dominant heating mechanism.

Photoelectric heating. — PE is caused by energetic stellar photons striking dust particles, ejecting electrons from the grains. Released electrons, in turn, contribute their kinetic energy to the gas. The PE heating rate per unit volume is given by Weingartner & Draine (2001)¹ as

$$\Gamma_{\text{PE}} = \int_{s_{\text{min}}}^{s_{\text{max}}} ds \frac{dn_{\text{dust}}}{ds} \pi s^2 \int_{(e\phi+W)/h}^{\nu_{\text{max}}} Q_{\text{abs}} Y(h\nu) \frac{F_{\nu}}{h\nu} d\nu \times \left[\int_0^{h\nu-W-e\phi} Ef(E, h\nu) dE \right]. \quad (1)$$

Here, $\int_{s_{\text{min}}}^{s_{\text{max}}} ds \frac{dn_{\text{dust}}}{ds} \pi s^2$ represents the total dust area per unit volume, coming from grains of radii between

s_{min} and s_{max} , that stellar photons can intercept. ϕ is the charging potential of the grain, W is its work function, Q_{abs} is the overall absorption coefficient, $Y(h\nu)$ is the photoelectric yield, F_{ν} is the stellar flux at a given frequency, E is energy of the ejected electrons, and $f(E, h\nu)$ describes their energy distribution. Following Weingartner & Draine (2001), we take $Q_{\text{abs}} = 1$. Throughout this paper we assume a carbonaceous composition for the dust grains, giving a work function of $W = 4.4$ eV. Also,

$$Y(h\nu) = \frac{E_{\text{high}}^2 (E_{\text{high}} - 3E_{\text{low}})}{(E_{\text{high}} - E_{\text{low}})^3} \times y_0, \\ f(E, h\nu) = \frac{6(E - E_{\text{low}})(E_{\text{high}} - E)}{E_{\text{high}}^2 (E_{\text{high}} - 3E_{\text{low}})}, \quad (2)$$

where $E_{\text{high}} = h\nu - W - e\phi$, $E_{\text{low}} = -e\phi$ and the dimensionless factor y_0 is the highly uncertain photoionization yield. Following Weingartner & Draine (2001), we take

$$y_0 = \frac{9 \times 10^{-3} (h\nu - W)^5}{W^5 + 3.7 \times 10^{-2} (h\nu - W)^5} \quad \text{carbonaceous,} \\ = \frac{0.5 (h\nu - W)}{W + 5(h\nu - W)} \quad \text{silicate.} \quad (3)$$

Each photoelectric electron that makes it out of the grain carries with it an average energy of order 1 eV.

The charging potential ϕ critically determines the heating capability of stellar photons – only stellar photons with energies above a threshold ($W + e\phi$) yield PE heating. The potential is independent of grain size and is obtained by equating the photoelectric charging current per unit area on the dust grain,

$$J_{\text{PE}} = \frac{e}{4} \int_{(e\phi+W)/h}^{\nu_{\text{max}}} Q_{\text{abs}} Y(h\nu) \frac{F_{\nu}}{h\nu} d\nu, \quad (4)$$

to the thermal electron collection current,

$$J_e = e s_e n_e \sqrt{\frac{k_B T_{\text{gas}}}{2\pi m_e}} \left(1 + \frac{e\phi}{k_B T_{\text{gas}}} \right). \quad (5)$$

Here $s_e \sim 0.5$ is the electron sticking coefficient, n_e is the electron density, obtained in our code from the ionization balance computation. T_{gas} is the gas temperature, m_e the electron mass and k_B the Stefan-Boltzman constant. Eq. [5] holds for positively charged grains ($e\phi > 0$), which is the case for debris disk gas densities (BW07). Also, as argued by Fernández et al. (2006), the charging potential depends logarithmically on disk parameters like electron density, gas temperature, etc.

Γ_{PE} depends directly on the area covered by the dust and through eq. [5] on electron density n_e . If we take the simplification that each liberated electron carries of order 1 eV of energy to the gas (second integral in eq. [1]), we can estimate $\Gamma_{\text{pe}} \approx \text{dust area} \times J_e \times 1 \text{ eV}/e \propto n_e$ (also see eq. [23]).

Also arising from eq. [5] is the dependence of PE heating on gas temperature, T_{gas} . Since $e\phi$ is generally a few $k_B T_{\text{gas}} \gg k_B T_{\text{gas}}$ (BW07), $e\phi/k_B T_{\text{gas}}$ is the dominant term in the equation. Hence, J_e (and in turn $\Gamma_{\text{PE}} \propto T_{\text{gas}}^{-1/2}$). At higher temperatures, the Coulomb focussing is weakened and electrons are less likely to be collected by the

¹ The Weingartner & Draine (2001) formulation is a refinement over that in Draine (1978). We adopt it here.

positively charged grains, hence $e\phi$ becomes more positive, thus raising the $W + e\phi$ threshold. As a result, the PE heating rate is reduced at higher gas temperatures. There is no runaway heating.

In practice, the double integrals of eq. [1] are pre-computed for a range of ϕ values. As the integrals are monotonic functions of ϕ , the value of ϕ is then obtained by equating the pre-computed thermal equilibrium calculation J_{PE} to J_e .

Gas-grain collisions.— The volumetric heating rate due to GG is given by eq. [19] in KvZ01

$$\Gamma_{\text{GG}} = 4.0 \times 10^{-12} \text{erg cm}^{-3} \text{s}^{-1} n_{\text{tot}} \alpha_T \sqrt{T_{\text{gas}}} \times (T_{\text{dust}} - T_{\text{gas}}) \int_{S_{\text{min}}}^{S_{\text{max}}} \pi s^2 \frac{dn_{\text{dust}}}{ds} ds, \quad (6)$$

where α_T is the thermal accommodation coefficient, taken to be 0.3. For $T_{\text{gas}} > T_{\text{dust}}$, gas-grain collisions cool the gas.

Heating due to photoionization.— The heating rate per unit volume due to photoionization is

$$\Gamma_{\text{PI}} = \sum_{i=1}^{30} \sum_{j=1}^3 \Gamma_{\text{E},i} n_{i,j}, \quad (7)$$

where $\Gamma_{\text{E},i}$ is the energy released per unit time, per unit atom (i) during photoionization, the subscript j denotes the ionization state. The photoionization rate is pre-computed for a given stellar flux and recalled when needed. We follow atoms H through Zn and through to their second ionization states (see Appendix for more details).

Heating due to Gas-Grain Drifting— Following BW07, we ignore drift heating due to differential velocity between gas and grains. This is justified in our problem where gas and grain are weakly coupled, and is also confirmed by the calculations of Gorti & Hollenbach (2004).

2.2. Cooling

When computing gas cooling, we include the fine structure lines O I 63.2, 44.1, 145.5 μm , C II 157.7 μm and Si II 34.8 μm , the atomic cooling lines O I λ 6300 \AA and Ly α , as well as free-free, and radiative recombination cooling.

For gas temperatures below 5000 K, O I, C II and Si II fine-structure transitions dominate the cooling (Hollenbach & McKee 1989). Collisionally excited levels decay spontaneously, converting thermal energy to photons that are lost to space, effectively cooling the gas. While both collisions with free electrons and atoms/ions can lead to fine-structure cooling, we neglect the latter since electrons move faster.

Cooling by fine-structure transitions.— Let n_i be the population density in level i . For sufficiently high electron densities (and therefore collision rates), each level is populated according to the local thermal equilibrium (LTE),

$$n_i = \frac{g_i \exp(-E_i/k_B T)}{\sum_i g_i \exp(-E_i/k_B T)} n_X, \quad (8)$$

where g_i is the statistical weight of state i , E_i its excitation energy, n_X the total number density of species X, and the summation runs through all energy levels. At

lower densities, a full statistical equilibrium calculation is required to determine n_i . The threshold densities ($n_{e,\text{crit}}$) between SE and LTE are listed in Hollenbach & McKee (1989) for various transitions. We collect values for lines of interest to this study in Table 1. The typical electron density encountered in our systems is of order twenty or less. As such, we have constructed the ONTARIO code to perform SE calculation for all elements of interest. In particular, for the important cooling elements (O I, C II and Si II), the SE calculation is self-consistently coupled to the gas thermal equilibrium calculation. Data required in such calculations, as well as the numbers of energy levels and transitions included, are detailed in the Appendix.

TABLE 1
RELEVANT COOLING LINES

Line	A_{ij} [s^{-1}]	$n_{e,\text{crit}}$ [cm^{-3}]
C II 157.7 μm	2.3×10^{-6}	$8.7 (T/100 \text{ K})^{0.50}$
O I 44.1 μm	8.9×10^{-10}	$6.3 \times 10^3 (T/100 \text{ K})^{-0.03}$
O I 63.2 μm	8.9×10^{-5}	$6.3 \times 10^3 (T/100 \text{ K})^{-0.03}$
O I 145.5 μm	8.9×10^{-10}	8.9×10^2
Si II 34.8 μm	2.1×10^{-4}	$1.2 \times 10^2 (T/100 \text{ K})^{0.50}$

NOTE. — $n_{e,\text{crit}}$ is the critical electron density above which LTE is approximately correct. T is gas temperature.

The line luminosity per unit volume for fine-structure de-excitation $i \rightarrow j$ is contributed by both spontaneous and stimulated emission,

$$F_{10} = [A_{ij} + B_{ij}(U_\nu)] n_i h\nu_{ij}, \quad (9)$$

where A_{ij} and B_{ij} are the usual Einstein coefficients, U_ν is the radiation field density at ν_{ij} . We ignore stimulated emission when computing line fluxes.² However, we do include the stellar fluxes and dust infrared radiation when computing SE. KvZ01 demonstrated that dust IR radiation promote population in the higher excitation states of O I, leading to stronger O I line fluxes.

The energy absorbed from radiation pumping leaves the system in two ways. Part of it is subsequently released as photons by spontaneous emission, part of it heats the gas via collisional de-excitation. The former process increases the line luminosity (as calculated in eq. [9]), but does not contribute to the net cooling of the gas. As a result, we define the gas cooling rate differently from the cooling line luminosity (eq. [9]) as the difference between collisional excitation and de-excitation between levels i and j ,

$$\Lambda_{ij} = (q_{ji} n_j - q_{ij} n_i) n_e h\nu_{ij}, \quad (10)$$

where q_{ji} and q_{ij} are collisional excitation and de-excitation rates, respectively. For very strong radiation fields in the vicinity of early-type stars, fluorescence can sometimes cause population inversion and lead to effective collisional *heating* of the gas.

² Photons arising from stimulated emission are highly anisotropic. In the case of stimulation by stellar photons, only emission from gas directly in our line-of-sight to the central star is detectable. Moreover, this contribution is negligible compared to spontaneous emission from the whole disk. We therefore decide to report only line fluxes from spontaneous emission.

O I (6300 Å) and Lyα transitions.— Electronic transitions only become important at high temperatures (eqs. [34] & [35] of KvZ01):

$$\Lambda_{O\text{I},\lambda 6300} = 1.8 \times 10^{-24} \text{ erg cm}^{-3} \text{ s}^{-1} n_{\text{O}} n_e \exp\left(-\frac{22\,800 \text{ K}}{T}\right)$$

$$\Lambda_{\text{Ly}\alpha} = 7.3 \times 10^{-19} \text{ erg cm}^{-3} \text{ s}^{-1} n_{\text{H I}} n_e \exp\left(-\frac{118\,400 \text{ K}}{T}\right)$$

Free-free cooling.— Free-free cooling also enters at high temperatures. Cooling due to electrons interacting with ions of charge Z is (eq. [3.14] in Osterbrock 1989)

$$\Lambda_{\text{ff}}(Z) = 1.42 \times 10^{-27} \text{ erg cm}^{-3} \text{ s}^{-1} g_{\text{ff}} Z^2 \sqrt{T} n_e n_+, \quad (13)$$

where n_+ is the ion number density and $g_{\text{ff}} \approx 1.3$ is the mean Gaunt factor for free-free emission. The total free-free cooling rate is the summation over all ionic species. The recombination cooling is similar to that in eq. [7], but with Γ_{E} replaced by Λ_{E} , the recombination cooling rate per electron for species i , and with $n_{i,j}$ replaced by electron number density n_e :

$$\Lambda_{\text{E}} = \sum_{i=1}^{30} \sum_{j=1}^3 \Lambda_{\text{E},i} n_e. \quad (14)$$

3. THE β PICTORIS DEBRIS DISK

In order to check the reliability of ONTARIO, we apply it to the well-studied debris disk of β Pictoris. The β Pic system is unique in that it is the only debris system where both the dust and the gas components have been extensively mapped (see, e.g., Chen et al. 2007, and references therein).

3.1. Input parameters

The adopted model parameters of the β Pic system are listed in Table 2. We used the same flux-calibrated stellar model spectrum for β Pic as in Fernández et al. (2006), except we merged the model spectrum with far- and near-ultraviolet observations from *FUSE* and *HST/STIS* (A. Roberge, priv. comm.), covering 925–1180 Å and 1465–1660 Å, respectively, and interpolating over the gap. The distribution of dust area is deduced from *HST/STIS* observations (Heap et al. 2000; Fernández et al. 2006) and summarized by a fitting form

$$\pi \langle a^2 \rangle n_{\text{dust}} = \frac{\tau_0}{W} \frac{\exp[-(z/W)^{0.7}]}{\sqrt{(\rho/\rho_0)^{-4} + (\rho/\rho_0)^6}}, \quad (15)$$

where ρ is the cylindrical radius and z the height above disk midplane. The empirically determined fitting parameters are $\rho_0 = 120$ AU, $W = 6.6(\rho/\rho_0)^{0.75}$ AU, and $\tau_0 = 2 \times 10^{-3}$. We also adopt the following form to describe the distribution of the total gas number density (Brandeker et al. 2004):

$$n_{\text{gas}}(\rho, z) = n_0 \left[\frac{2}{(\rho/\rho_1)^{2\alpha_1} + (\rho/\rho_1)^{2\alpha_2}} \right]^{1/2} \exp\left[-\frac{z^2}{2\sigma_z^2}\right]. \quad (16)$$

For elemental abundances, we assume solar abundances (Grevesse & Noels 1993) except for three elements: hydrogen is set to 10^{-3} of its solar value, helium is assumed to be zero, and carbon is set to be $20\times$ its solar

abundance. This is motivated below. We then compare our model output to the observed Na I profile to obtain values for the fitting parameters, $\rho_1 \approx 100$ AU, $\alpha_1 = 1.0$, $\alpha_2 = 2.3$, $n_0 = 24 \text{ cm}^{-3}$, $\sigma_z = (\rho/100 \text{ AU}) \times 10 \text{ AU}/\sqrt{8 \ln 8}$. This derived distribution is similar to that in eq. [4] of Brandeker et al. (2004) except for two differences: our n_0 is a factor of 10^3 smaller as we adopt a hydrogen poor mix while they assumed a solar abundance of hydrogen; our vertical distribution is well approximated by a Gaussian profile with a full width half maximum (FWHM) of $H = 0.4r$. This differs from Brandeker et al. (2004) because we include the variation of ionization fraction with height in this work, while Brandeker et al. (2004) did not.

The volume density of dust area (eq. [15]) vanishes close to the star, indicating an inner clearing of dust. The gas profile of the inner disk is uncertain. The Na I emission line can be traced in to a projected separation of 13 AU from the star and out to 323 AU from the star. Comparing the Na I seen in emission with the Na I seen in absorption, Brandeker et al. (2004) concludes that 80–100% of the circumstellar Na I seen in absorption is within this range. We therefore limit the gas disk to start at 15 AU and end at 200 AU (with more distant regions making negligible contributions to the total line luminosities). The model disk height is limited to 100 AU above the midplane.

To relate the dust opacity distribution of eq. [15] to the dust disk mass, we assume that dust grains are spherical and range in sizes $s_{\text{min}} < s < s_{\text{max}}$, with a differential number distribution $dn_{\text{dust}}/ds \propto s^{-3.5}$, as characteristic of dust in the interstellar medium. s_{max} is set, somewhat arbitrarily, to 1 cm, while s_{min} is set to be the minimum size below which radiation pressure could remove the grains. For a grain initially at circular orbit, this occurs when the ratio of the radiation pressure to gravitational force acting on the grains, β , is equal to 0.5. This translates to

$$s_{\text{min}} = \frac{3L_{\star} Q_{\text{PR}}}{16\pi GM_{\star} c \varrho_{\text{grain}} \beta} = \frac{3L_{\star} Q_{\text{PR}}}{8\pi GM_{\star} c \varrho_{\text{grain}}}, \quad (17)$$

where c is the speed of light and $Q_{\text{PR}} \sim 1$ is the radiation pressure efficiency averaged over the stellar spectrum. For β Pic, we assume $M_{\star} = 1.75 M_{\odot}$ and $L_{\star} = 11 L_{\odot}$. Taking $\varrho_{\text{grain}} \sim 1 \text{ g cm}^{-3}$, we find $s_{\text{min}} \sim 5 \mu\text{m}$.

The infrared luminosity from the dust, integrated over the whole disk, is thus given by:

$$L_{\text{dust}} = \iint \frac{L_{\star}}{4\pi(\rho^2 + z^2)} (1 - \epsilon) \pi \langle a^2 \rangle n_{\text{dust}} 2\pi \rho \, d\rho dz, \quad (18)$$

where $\epsilon \sim 0.5$ is the grain reflectivity coefficient. When using the β Pic dust distribution described by eq. [15], $L_{\text{dust}} \sim 10^{-3} L_{\star}$.

To derive the grain temperature as a function of distance from the star, we use an empirical relation derived from observations of the β Pic dust disk. From observations (e.g. Nilsson et al. 2009) it is clear that the dust cannot radiate as black bodies, as that would imply too much sub-mm radiation. Instead, the spectral energy distribution of the disk is found to be well fit by a mod-

ified black body,

$$I_\nu = \left(\frac{\nu}{\nu_0}\right)^\gamma B_\nu(T). \quad (19)$$

One can attempt to relate γ and ν_0 to dust properties (e.g. Draine 2003), but that is beyond the scope of the present article, where we are content that this simple empirical relation approximates the observed dust emission surprisingly well. Using eq. [19] for radiative equilibrium, where we equate the absorbed energy flux to the emitted, we get

$$\frac{(1-\epsilon)L_\star}{4\pi R^2} \pi a^2 = 4\pi a^2 \int_0^\infty \pi \left(\frac{\nu}{\nu_0}\right)^\gamma B_\nu(T),$$

which in turn implies

$$T = \frac{(1-\epsilon)L_\star \nu_0^2 c^2}{32h\pi^2 R^2 \zeta(4+\gamma)\Gamma(4+\gamma)},$$

where ϵ is an average albedo for stellar radiation, L the luminosity of the star, h is Planck's constant, c speed of light, ζ is the Riemann ζ -function, and Γ the (true) gamma function. Using eq. [21] to compute the temperatures the β Pic dust disk, and eq. [19] the dust area density distribution of eq. [15] to compute the emission, we integrate the total emission from disk seen at Earth to fit $\gamma = 0.67$ and $\nu_0 = 4 \times 10^{14}$ by comparing to the SED summarized in Nilsson e (2009). A simplified expression for the dust temperature is thus

$$T \approx 430 \text{ K} \left(\frac{L_\star}{L_\odot}\right)^{0.214} \left(\frac{R}{\text{AU}}\right)^{-0.428} \left(\frac{\nu_0}{4 \times 10^{14} \text{ Hz}}\right)^0$$

Returning back to the issue of elemental abundances, observations and numerical modeling of gas in the β Pic system indicate that the disk may be deficient in hydrogen, consistent with a disk comprised of mainly metals, produced as a result of dust sublimation (Lecavelier des Etangs et al. 2001; Brandeker et al. 2004; Fernández et al. 2006). In addition, the gas in the disk has been found to be of $20\times$ higher carbon abundance than expected for solar composition (Roberge et al. 2006). Other observed elements are close to solar in relative abundance. The abundance of oxygen, which is important for cooling the gas, is unfortunately hard to constrain, because the available absorption lines are strongly saturated (Roberge et al. 2006), although a solar abundance is consistent with data. Consequently, for our study, we set all elemental abundances at their solar values except for carbon at 20 times solar, hydrogen at 10^{-3} solar and helium abundance set to zero.

3.2. Comparing the model to observations

3.2.1. Disk temperature profile

Fig. 2 shows β Pic disk midplane gas and dust distribution and temperature profiles together with important heating and cooling mechanisms. The temperature in the disk is determined by two major heating mechanisms: PE and PI heating. PE is maximum around 100 AU where the dust distribution peaks; PI dominates in the strong radiation field within ~ 25 AU of the star. With low gas densities gas-grain collision rates are negligible,

TABLE 2
 β PIC DISK MODEL INPUT PARAMETERS

M_\star	$1.75 M_\odot$
R_\star	$2 R_\odot$
L_\star	$11 L_\odot$
Disk inner cutoff	15 AU
Dust mass	$0.27 M_\oplus$
Dust profile	eq. [15]
Dust luminosity	$9.6 \times 10^{-4} L_\star$
Gas mass	$8.3 \times 10^{-4} M_\oplus$
Gas profile	eq. [16]

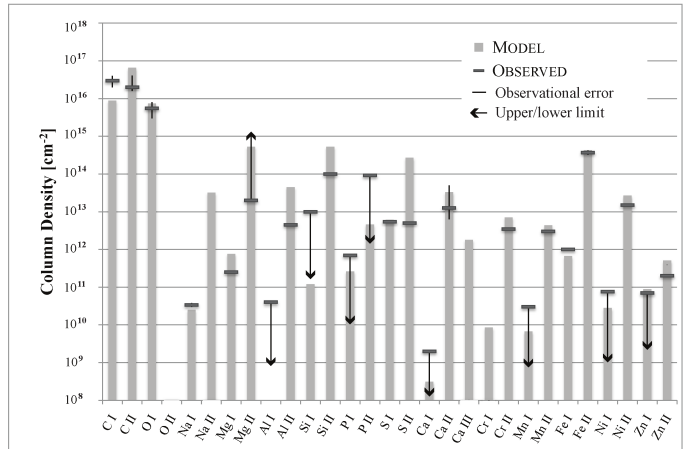


FIG. 1.— Column densities for metallic gas in the β Pic disk, same data as in Tab. 3. No data for O II, Na II, Ca III, Cr I are available as these are not observed in optical spectra. Na I and Fe II are strongly constrained, and no observational uncertainty data are available for Mg I, Al II, Si II, S I, S II, Cr II, Mn II, Fe I, Ni II, Zn II.

so that gas and dust temperatures are effectively decoupled. The result is a gas temperature profile that peaks at the inner disk boundary and at 100 AU. The cooling is dominated almost exclusively by the C II $157.7 \mu\text{m}$ fine structure transition. The Si II line transition becomes stronger in the higher temperature region around dust distribution peak, yet still remains ~ 100 times below the C II flux.

3.2.2. Column densities

The edge-on orientation of the β Pic disk makes it possible to observe the disk gas through absorption. In Table 3 we list column densities inferred from observations and column densities computed with ONTARIO, using the disk model outlined in § 3.1. The same comparison is also presented in Fig. 1 for better visualization.

The real gas disk is far from being cylindrically symmetric, with the observed Na I profiles from the southwest (SW) and north-east (NE) parts of the β Pic disk differing substantially. The NE side is the brightest within a projected distance of 35 AU and outside 100 AU, and is detected to the limit of the observations at 323 AU. The SW side on the other hand, is slightly brighter in the 35–100 AU region, and drops much more quickly outside 100 AU than the NE side (Fig. 3 of Brandeker et al. 2004). Given that the model is based on the spatially resolved emission from the Na I D₂ line, where the

TABLE 3
COLUMN DENSITIES FOR METALLIC GAS IN THE β PIC DISK

Species	Observed [cm^{-2}]	Model [cm^{-2}]
C I	$(2-4) \times 10^{16}$	8.9×10^{15}
C II	$2.0^{+2.1}_{-0.4} \times 10^{16}$	6.6×10^{16}
O I	$(3-8) \times 10^{15}$	7.4×10^{15}
O II	...	0.0
Na I	$(3.4 \pm 0.4) \times 10^{10}$	2.5×10^{10}
Na II	...	3.2×10^{13}
Mg I	2.5×10^{11}	7.6×10^{11}
Mg II	$\geq 2 \times 10^{13}$	5.3×10^{14}
Al I	$\leq 4 \times 10^{10}$	1.0×10^8
Al II	4.5×10^{12}	4.5×10^{13}
Si I	$\leq 1 \times 10^{13}$	1.2×10^{11}
Si II	1×10^{14}	5.3×10^{14}
P I	$\leq 7.0 \times 10^{11}$	2.6×10^{11}
P II	$\leq 9.2 \times 10^{13}$	4.6×10^{12}
S I	5.4×10^{12}	6.1×10^{12}
S II	5×10^{12}	2.7×10^{14}
Ca I	$\leq 2 \times 10^9$	3.1×10^8
Ca II	$1.26^{+3.75}_{-0.63} \times 10^{13}$	3.3×10^{13}
Ca III	...	1.8×10^{12}
Cr I	...	8.5×10^9
Cr II	3.5×10^{12}	7.1×10^{12}
Mn I	$\leq 3 \times 10^{10}$	6.7×10^9
Mn II	3×10^{12}	4.4×10^{12}
Fe I	1×10^{12}	6.7×10^{11}
Fe II	$(3.7 \pm 0.5) \times 10^{14}$	4.3×10^{14}
Ni I	$\leq 7.6 \times 10^{10}$	2.8×10^{10}
Ni II	1.5×10^{13}	2.7×10^{13}
Zn I	$\leq 7 \times 10^{10}$	8.9×10^{10}
Zn II	2×10^{11}	5.1×10^{11}

NOTE. — Observed column densities are compiled by Roberge et al. (2006). Some species are unconstrained, as no absorption line has been observed. The column density of Mg II is to be considered a lower limit since the line is strongly saturated.

Na I represents only 10^{-3} of the total Na, the agreement in column density between observation and prediction is remarkable, and reinforces the conclusion by Brandeker et al. (2004) that the gas seen in absorption is the same seen in emission.

The model predicts most elements to be highly ionized, with the exceptions of O and C, due to their higher ionization potential. Only a few elements have their ionization fractions directly determined (as an column density average), but many have ionization fractions constrained by the data. Overall, the predicted ionization levels from ONTARIO are consistent with observations, with the exception of C and S, which appear less ionized than predicted. Interestingly, together with the elements O and P (which do not have their ionization level observationally constrained), these are the elements of Table 3 with the highest ionization potential (first ionization potentials are 10.4 [for S], 11.3 [C], 13.6 [O], and 10.5 eV [P]). Their ionization fractions are thus the most sensitive to the stellar UV spectrum at energies higher than 10 eV. A possibility for the discrepancy is thus that the UV flux in our adopted stellar spectrum is overestimated compared to the actual spectrum.

There is the tantalizing possibility of doing cosmochemistry using these data. If indeed the metallic gas arises from grain-grain collisions, the evaporated gas could have the same chemical composition as the grains. This provides a window to study the make-up of β Pic's

planetesimal belt, much like what cosmochemists have accomplished by studying meteorites that fall on Earth. Among the intriguing questions to ask are: why is C so super-solar, and is the factor of 10 depletion observed in Al significant?

3.2.3. Cooling line fluxes

As outlined in § 2.1, we can estimate the total cooling line fluxes by estimating the PE heating rate. Assuming that every escaping electron heats the gas by ~ 1 eV, we obtain the following order-of-magnitude estimate for the cooling luminosity,

$$\begin{aligned}
 L_{\text{cool}} &\sim \int dV \Lambda_{\text{fine}} \approx \int dV \Gamma_{\text{pe}} \\
 &\approx \int dV \int_{s_{\text{min}}}^{s_{\text{max}}} ds \frac{dn_{\text{dust}}}{ds} \pi s^2 \times \frac{J_e}{e} \times 1 \text{ eV} \\
 &\sim \frac{2L_{\text{dust}}}{L_*} \times 4\pi R^2 \times \frac{J_e}{e} \times 1 \text{ eV} \\
 &\sim 10^{-8} L_{\odot} \left(\frac{T_{\text{gas}}}{100 \text{ K}} \right)^{-1/2} \left(\frac{R}{100 \text{ AU}} \right)^2 \\
 &\quad \times \left(\frac{L_{\text{dust}}/L_*}{10^{-3}} \right) \left(\frac{n_e}{20 \text{ cm}^{-3}} \right) \left(\frac{e\phi}{2 \text{ eV}} \right), \quad (23)
 \end{aligned}$$

where the factor of 2 in front of L_{dust} corrects for albedo, and R is the radius of the dust ring. This estimate roughly explains the total cooling luminosity of $\sim 7 \times 10^{-8} L_{\odot}$ we obtain for β Pic (Table 4), and it illuminates the dependency of cooling luminosity on gas and dust properties.

We compare these values to a previous model by BW07, also shown in Table 4. The total cooling luminosity there is higher by a factor of 30 and the dominant line is O I 63.2 μm line, as opposed to the C II 157.7 μm line here. These are explained by the three major differences between the model we adopt here and that adopted by BW07: 1) the gas mass (the metallic component) adopted in BW07 is about seven times greater than we use here. As they also include contribution to electron density from hydrogen, the total electron density is some fifteen times greater than our value (see eq. [23]). 2) BW07 used LTE to compute the level occupation, while we calculate the detailed statistical equilibrium (SE). For the low electron density in the β Pic disk ($n_e \sim 20 \text{ cm}^{-3} \ll n_{e,\text{crit}}$ for some ions), an LTE treatment grossly overestimate the occupation number in the excited states of O I. This accounts for their strong O I lines. In our β Pic model, oxygen atoms do not contribute to cooling significantly. To test that there are no other significant differences between ONTARIO and the model used by BW07, we used their gas and dust distribution and enforced LTE for the level populations, and confirmed that these changes made ONTARIO reproduce the BW07 results.

For the β Pic dust and gas profiles, turning off the dust IR field in our code only produces a $< 4\%$ variation on the O I 63.2 μm line flux.

Our predicted value for the C II 157.7 μm line flux is high enough to be detectable with heterodyne far-infrared spectrometer *HIFI* on *Herschel*. For a crude estimate of the instruments sensitivity, we use the pre-launch predicted sensitivity, expressed as the system

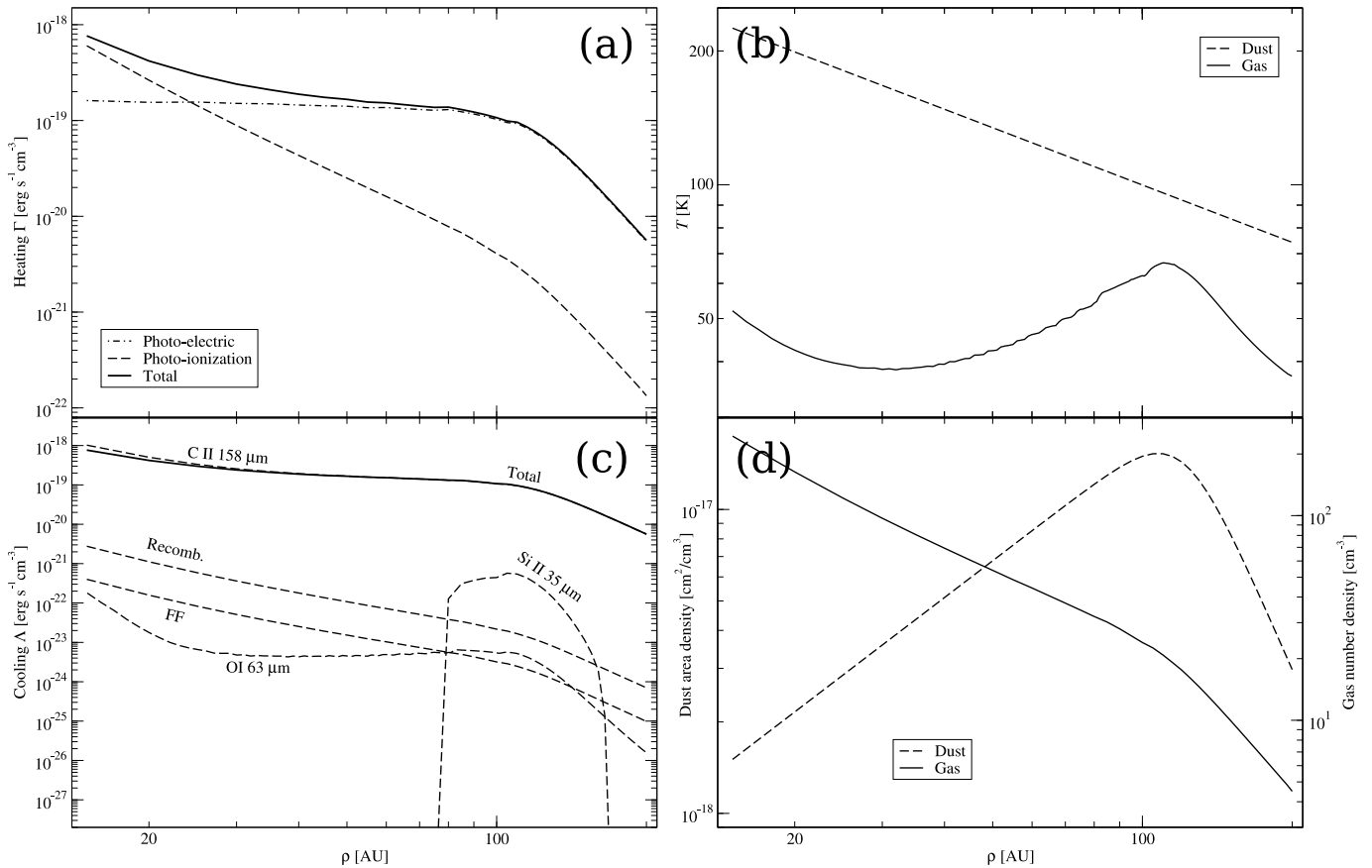


FIG. 2.— Physical properties of the β Pic midplane in our model. The upper left panel (a) shows the few important heating rates, and the lower left panel (c) the dominant cooling rates. The upper right panel (b) shows the gas and dust temperatures, respectively, and the lower right panel (d) gas and dust densities (note different scales and units for the two populations).

TABLE 4
 β PIC COOLING LINE LUMINOSITIES

Line	ONTARIO output			BW of 10^{-13} erg cm^{-2} s^{-1} (4σ result)
	Luminosity	Flux	Flux (no dust IR)	
	[L_{\odot}]	[erg s^{-1} cm^{-2}]	[erg s^{-1} cm^{-2}]	[erg s^{-1} cm^{-2}]
C II 157.7 μm	9.0×10^{-8}	7.2×10^{-15}	7.2×10^{-15}	6.0×10^{-15}
O I 44.1 μm	1.9×10^{-15}	1.5×10^{-22}	1.5×10^{-22}	7.7×10^{-23}
O I 63.2 μm	7.1×10^{-10}	5.7×10^{-17}	5.5×10^{-17}	2.1×10^{-17}
O I 145.5 μm	7.3×10^{-11}	5.9×10^{-18}	5.9×10^{-18}	3.1×10^{-18}
Si II 34.8 μm	5.6×10^{-9}	4.5×10^{-16}	4.5×10^{-16}	3.1×10^{-16}

NOTE. — Luminosities and fluxes of the important cooling lines, as observed on Earth, computed by ONTARIO. To estimate the contribution from the dust IR field, cooling line fluxes without dust IR field are included.

temperature $T_{\text{sys}} = 2000$ K at 157.7 μm . Assuming the emission to be unresolved at a nearly diffraction-limited beam-size of $12''$, a flux of 7.2×10^{-15} erg s^{-1} cm^{-2} corresponds to the velocity integrated antenna temperature 0.38 K km s^{-1} . Assuming the line to be 10 km s^{-1} broad, i.e. the frequency bandwidth $\Delta\nu = 60$ MHz, the effective integration time required for a 5σ -detection should be on the order of

$$t \sim \frac{1}{6 \times 10^7 \text{ Hz}} \left(\frac{5 \times 10 \text{ km s}^{-1} \times 2000 \text{ K}}{0.38 \text{ K km s}^{-1}} \right)^2 = 20 \text{ min.} \quad (24)$$

The line could also be detected by *PACS* on *Herschel*,

with a similar effective integration time.

A tentative detection of the C II 157.7 μm line was reported for the β Pic disk (Kamp et al. 2003) with a flux of 10^{-13} erg cm^{-2} s^{-1} (4σ result). This is more than $10\times$ stronger than our prediction and a confirmation by *Herschel* is necessary (we estimate it would be confirmed with a 5σ confidence in ~ 6 seconds of integration time). Unfortunately, the O I 63.2 μm emission predicted by our model (5.7×10^{-17} erg s^{-1} cm^{-2}) is far too weak to be detected by *PACS*, which has a pre-launch estimated sensitivity of 10^{-15} erg s^{-1} cm^{-2} (5σ , 1 h). The wavelength region of Si II 34.8 μm line is not covered by any present or planned instrument and, as such, cannot be confirmed.

4. LINE LUMINOSITIES FROM DISKS AROUND A AND F STARS

Having studied the β Pic disk in some detail, we now proceed to investigate a range of potential debris disk configuration. We first study a fiducial disk with parameters tuned to resemble the β Pic disk of §3, but with simplified gas and dust profiles. We then investigate the temperature and ionization rates in the disk, fine-structure cooling line fluxes, and identify major emission and absorption lines. We vary these parameters systematically and report their influences on the observed cooling fluxes. In particular, we sample changes in elemental abundances (C, O, and H), variations in the total mass and distribution of gas and dust in the disk, and test a

range of stellar spectral types.

4.1. Fiducial disk

TABLE 5
FIDUCIAL CASE INPUT PARAMETERS

M_*	$1.75 M_\odot$
R_*	$2 R_\odot$
L_*	$11 L_\odot$
Dust mass	$0.5 M_\oplus$ (assuming a bulk density of 1 g cm^{-3} and $s_{\text{max}} = 1 \text{ cm}$)
Dust profile	eq. [25]: $\rho_{0,\text{dust}} = 120 \text{ AU}$, $\text{FWHM}_\rho = 10 \text{ AU}$ $H/\rho = 0.1$, $n_{0,\text{dust}} = 2.9 \times 10^{-16} \text{ cm}^2 \text{ cm}^{-3}$
Dust size distribution	$dn_{\text{dust}}/ds \propto s^{-3.5}$, $s_{\text{min}} \leq s \leq 1 \text{ cm}$
Gas mass	$3.0 \times 10^{-4} M_\oplus$
Gas profile	eq. [25]: $n_{0,\text{gas}} = 24 \text{ cm}^{-3}$, $\rho_{0,\text{gas}} = 100 \text{ AU}$, $\text{FWHM}_\rho = 40 \text{ AU}$, $H/\rho = 0.4$
Elemental abundances	solar (Grevesse & Noels 1993), except [C] = 20 [C] $_\odot$, [H] = 10^{-3} [H] $_\odot$ and [He] = 0

Fiducial case input parameters are listed in table 5. For the gas distribution observed in the β Pic system (eq. [16]), the total mass of the gas disk depends not only on the parameters specifying the gas profile, but also on the choice of inner and outer disk boundaries. To avoid this complication, we choose a double-Gaussian profile for both the gas and the dust components,

$$n = n_0 \exp \left[-\frac{(\rho - \rho_0)^2}{2\sigma_\rho^2} \right] \exp \left[-\frac{z^2}{2\sigma_z^2} \right]. \quad (25)$$

Here ρ and z are cylindrical coordinates, $\sigma_\rho = \text{FWHM}_\rho/\sqrt{8 \ln 2}$ represents the width of the radial distribution and $\sigma_z = (\rho/\rho_{\text{ref}}) \times \text{FWHM}_z/\sqrt{8 \ln 2}$ is the vertical profile width that scales linearly with distance. At $\rho_{\text{ref}} = 100 \text{ AU}$ we set FWHM_z to 40 AU , giving a constant $H/\rho = 0.4$. The peak midplane density $n_{0,\text{gas}}$ is set to 24 cm^{-3} , based on the value observed for the β Pic system. The interstellar medium gas density of $6.7 \times 10^{-3} \text{ cm}^{-3}$ is chosen as a lower limit throughout the disk, should the Gaussian of eq. [25] fall below this ($6.7 \times 10^{-3} \text{ cm}^{-3}$ corresponds to 1 cm^{-3} if solar abundances of H and He were to be included). The Gaussian distribution of the dust is slightly offset from the gas in the radial direction (see Fig. 3) with a steeper radial and vertical drop-off (FWHM_ρ of 10 AU and $H/\rho = 0.1$).

The implied dust luminosity is $1.2 \times 10^{-3} L_*$. To convert between the dust area distribution and the total dust mass, we computed s_{min} from eq. [17].

4.1.1. Disk temperature profile

Fig. 3 shows the gas and dust temperature obtained in our fiducial model, as well as various cooling and heating rates. The gas is thermally decoupled from the dust, as the low gas-grain collision rate is not able to equilibrate the two population. We find that PE heating dominates the gas heating where dust density is high, and that PI heating dominates where dust density is relatively low. Over most of the disk, cooling is dominated by the C II $157.7 \mu\text{m}$ line. However, as gas temperatures rises above $\sim 100 \text{ K}$, the cooling flux of C II saturates as the upper occupation number n_1 approaches the LTE limiting

value, $n_1 \rightarrow g_1/(g_0 + g_1)n_0$. Other cooling lines come into importance, including the Si II $34.8 \mu\text{m}$ line, the Ly α line, and gas-grain collisions. The O I lines, estimated to be important by BW07, are insignificant in our model, due to NLTE effects.

Fig. 3 shows the gas temperature at the peak of the dust distribution to rise as high as $2.5 \times 10^4 \text{ K}$. Since ON-TARIO does not include some cooling processes becoming important above 5000 K (like C I $\lambda 9849$, C II $\lambda 2324$, Fe II $1.26 \mu\text{m}$, etc. Hollenbach & McKee 1989), this is an overestimate.³ There is a possibility, however, that the temperature is high enough for the gas to thermally evaporate. Let the criterion be that the sound speed (for Carbon) becomes comparable to the orbital escape velocity:

$$T_{\text{max}} = 1.7 \times 10^4 \left(\frac{r}{100 \text{ AU}} \right) \text{ K}. \quad (26)$$

As this temperature limit is below our (over-)estimate, we cannot rule out gas evaporation from the disk; a more detailed study, outside the scope of the present paper, would be required.

4.1.2. Cooling line fluxes

Table 6 lists cooling line luminosities integrated over the whole disk for the fiducial case. C II $157.7 \mu\text{m}$ remains the most luminous line, with Si II $34.8 \mu\text{m}$ following within an order of magnitude, while O I lines are very underluminous compared to previous study (Besla & Wu 2007) due to NLTE effects. Most of the line flux is generated in region of highest gas and dust densities: 93% of the total C II $157.7 \mu\text{m}$ flux arises in the region extending radially from 100 to 140 AU and vertically up to 20 AU .

For C II, which is close to LTE, the line flux is dominated by collisional processes (eq. [9] \approx eq. [10]), which in turn is determined by the heating processes (in this case, photoelectric heating). Compared to the β Pic case, the fiducial case has a higher gas temperature in the dust maximum and consequently a smaller photoelectric heating rate. This explains largely the lower C II flux in the latter. This difference is further compounded by enhanced photoionization heating in the β Pic case due to a larger amount of gas closer to the star. O I, on the other hand, experiences an electron density that falls far below its critical density for LTE and its line flux arises largely from excitation by stellar photons (radiative pumping) and not collisional excitation which leads to cooling. This is reflected in the third column of Table 6, which shows that the cooling fraction (fraction of the line flux responsible for cooling the gas, the ratio of eq. [10] to eq. [9]) for O I is $0.06 \ll 1$, while it is 0.96 for C II.

4.1.3. Ionization profile

In our fiducial model, the metallic gas is strongly ionized by the central star. Figs. 4 & 5 show the neutral fractions of Ca, Na, and C, the main contributors to the electron density. We also show the fractions of Ca II and Ca III since a significant fraction of Ca is ionized a second time.

³ However, our tests indicate that at the low gas density assumed here, these cooling mechanisms are negligible even at temperatures as high as 10^5 K .

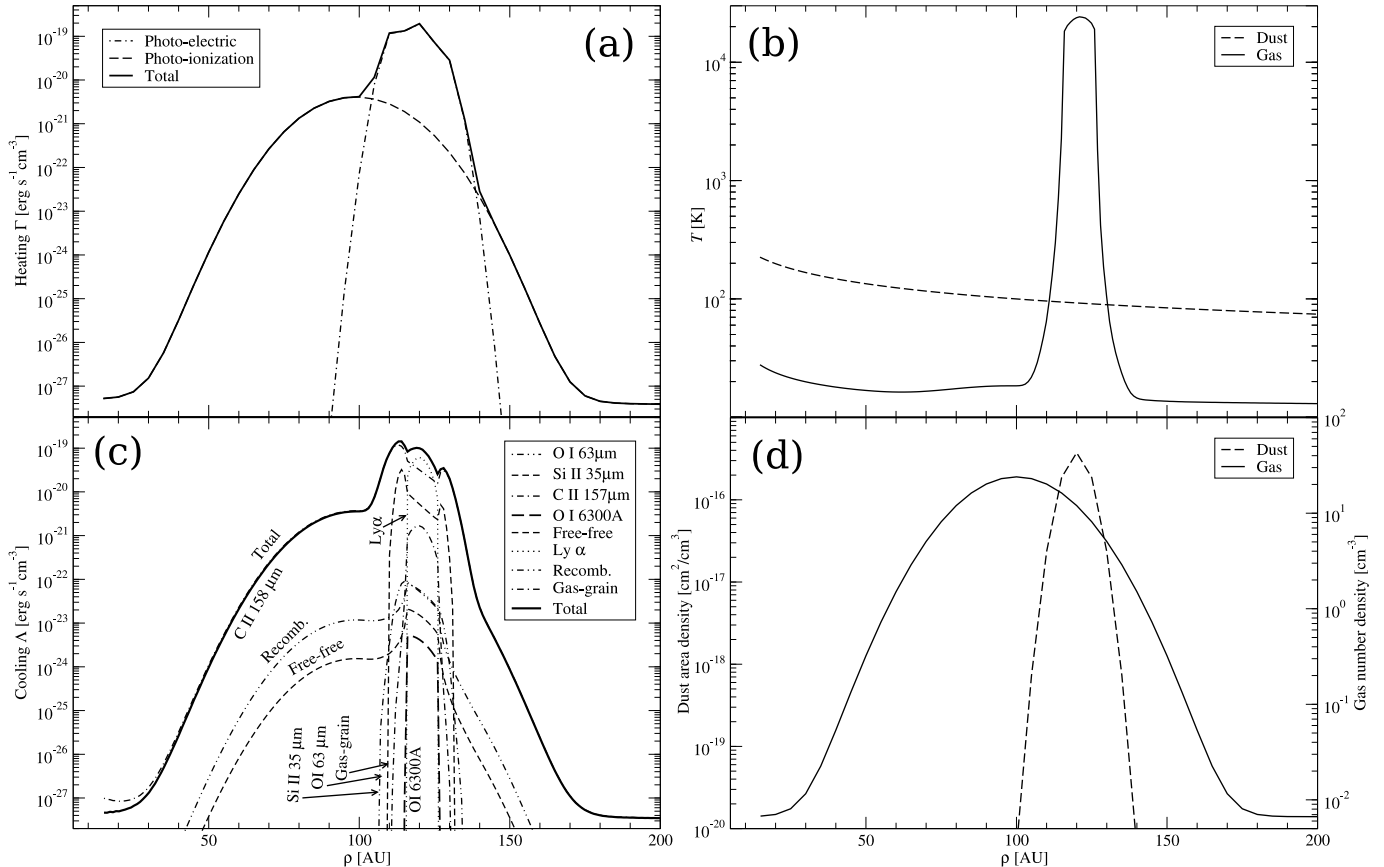


FIG. 3.— Similar to Fig. 2, but for the fiducial model. Due to the higher $n_{\text{dust}}/n_{\text{gas}}$ value at the dust peak, the gas temperature there experiences a spike and rises beyond 5000 K (see § 4.1.1 for discussion).

TABLE 6
FIDUCIAL CASE COOLING LINE LUMINOSITIES

Line	Luminosity [L_{\odot}]	Flux at 20 pc [$\text{erg s}^{-1} \text{cm}^{-2}$]	Cooling Fraction ^a
C II 157.7 μm	2.3×10^{-8}	1.8×10^{-15}	0.96
O I 44.1 μm	3.5×10^{-16}	2.8×10^{-23}]
O I 63.2 μm	1.5×10^{-10}	1.2×10^{-17}	0.06 ^b
O I 145.5 μm	1.4×10^{-11}	1.1×10^{-18}]
Si II 34.8 μm	3.2×10^{-9}	2.6×10^{-16}	0.63

NOTE. — Cooling line luminosities and fluxes measured at 20 pc, as predicted by ONTARIO for the fiducial model.

^aFraction of line luminosity from collisional processes (the ratio of eq. [10] to eq. [9]); the remainder is due to radiative pumping and does not contribute to cooling of the gas.

^bTotal O I cooling fraction summed over all 3 transitions.

The ionization profile is explained by a competition between stellar photoionization and recombination. Rate for the former falls off as one moves away from the star, while rate for the latter scales with electron density (and weakly depends on temperature through the recombination coefficient). So the neutral fraction is the lowest near the star and it rises upward until it reaches a maximum around 100 AU. Outward of this distance, the sharp drop of gas density reduces the recombination rate faster than the decrease of the ionization rate, resulting again in a more ionized gas. The neutral fractions exhibit a narrow dip at around 120 AU. This is due to the temperature peak (as shown in Fig. 3), which in turn is due to the dust peak at that location. As is seen in Fig. 5, the

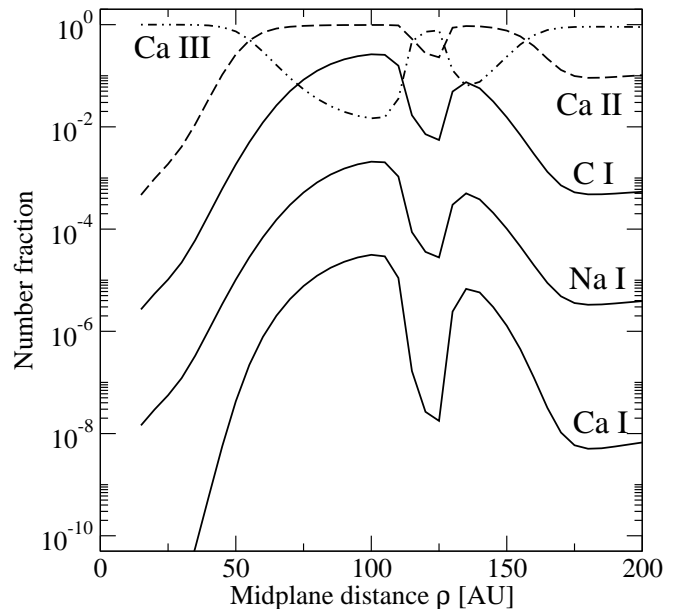


FIG. 4.— Midplane neutral (unbroken line) and ionization (dashed for one time ionized, and dash-dotted for two times ionized) fractions of three selected elements: Ca, Na, and C.

neutral fractions decrease monotonically away from the midplane due to the reduction in recombination in lower densities.

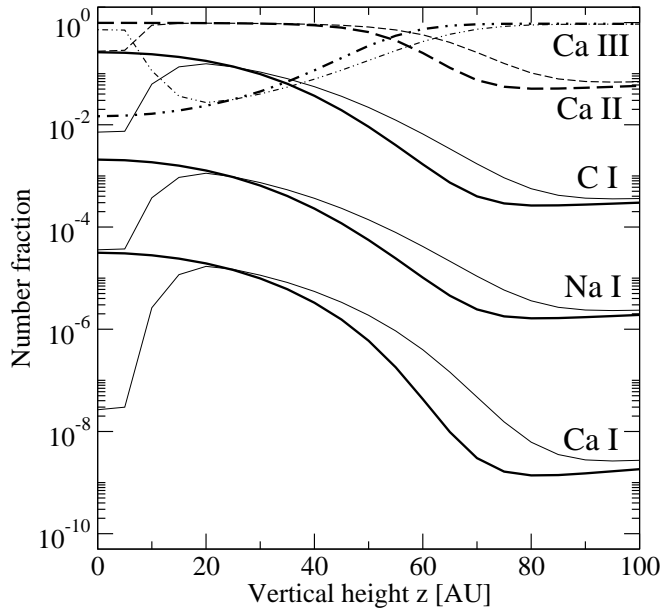


FIG. 5.— As in Fig. 4, but for the vertical distribution at 100 AU (thick line) and 120 AU (thin line).

4.1.4. Optical/UV absorption and emission lines

Observationally, an advantage of the IR cooling lines is that the stellar photosphere is relatively dark at those wavelengths, making faint emission lines more easily detectable. Should the disk be spatially resolvable or be observed edge on, strong transitions in the optical/UV might still be easier to detect. Indeed, gas around β Pic was first detected in absorption (Slettebak 1975; Hobbs et al. 1985), and then in spatially resolved emission from light scattered in atomic resonance lines (Na I D_{2,1}; Olofsson et al. 2001); apart from the tentative detection of C II 157.7 μ m emission (Kamp et al. 2003), cooling lines have yet to be observed from the disk. With this in mind, we have computed equivalent widths for absorption lines assuming an edge-on disk (Table 7), and total luminosities for light scattered in lines with strong transitions (Table 8). Resolved observations of the Ca II K absorption line around β Pic (Crawford et al. 1998) show it to be $\sim 2 \text{ km s}^{-1}$ wide. We assume absorption from the ‘stable component’ of other species to be similarly broadened, resulting in increasing saturation for lines with equivalent widths approaching 2 km s^{-1} .

4.2. Parametric survey

To detect circumstellar gas in absorption requires a special geometry, and to detect light scattered in gas most likely requires a resolved disk. A comprehensive survey for tenuous gas in debris disks is therefore best served by the IR cooling lines. In this section, we study how the cooling line luminosities depend on various disk parameters, focusing on the C II 157.7 μ m and O I 63.2 μ m lines, since these fall in the wavelength window of the Herschel telescope. The parameter study is obtained by modifying one parameter at a time while keeping all other parameters at their fiducial values. Disk parameters and their ranges (provided for easy reference in Table 9) that we cover include:

TABLE 7
FIDUCIAL CASE DOMINANT ABSORPTION LINES

Species	$\lambda_{\text{vacuum}}^{\text{a}}$ [Å]	Eq. Width ^b [mÅ]
Na I	5891.58	0.86
Na I	5897.56	0.43
Ca II	3934.78	OT
Ca II	3969.59	OT
Ti II	3350.37	0.82
Ti II	3362.18	0.59
Ti II	3373.77	0.51
Ti II	3384.74	0.39
Mn II	3442.97	0.15
Fe I	3441.59	0.31
Fe I	3720.99	0.88
Fe I	3735.93	0.36
Fe I	3861.01	0.53

^aOnly lines with $\lambda \geq 3300 \text{ Å}$ are presented.

^bOT - optically thick line, defined to have an equivalent width that corresponds to a velocity $\gtrsim 2 \text{ km s}^{-1}$.

1. peak gas density. Range covered is from 0.01β Pic density ($2.4 \times 10^{-1} \text{ cm}^{-3}$) to $\sim 2.7 \times 10^3 \text{ cm}^{-3}$, the latter corresponds to a column density above which the C II 157.7 μ m line becomes radially optically thick. For the spatial distribution we adopt, these densities correspond (through eq. [25] with fiducial parameters) to a total gas masses of $2.1 \times 10^{-6} M_{\oplus}$ and $3.3 \times 10^{-2} M_{\oplus}$, respectively.
2. total dust mass. We sample dust mass from 1 zodiac (taken as $M_{\text{dust}} = 10^{-3} M_{\oplus}$; with fiducial disk parameters, this corresponds to $L_{\text{dust}}/L_{*} \sim 10^{-6}$) to $3 M_{\oplus}$, at which point the dust becomes radially optically thick (with $L_{\text{dust}}/L_{*} \sim 3 \times 10^{-3}$).
3. spatial distributions of the gas and dust components, including location of peak density, radial FWHM and vertical scale height, spanning about an order of magnitude in each parameter.
4. elemental abundances. We vary carbon and oxygen abundances, respectively, from solar to $20\times$ solar, to account for the type of abundance anomaly detected in the β Pic disk.
5. stellar spectral type. We study main sequence stars with effective photosphere temperatures ranging from 6500 K to 10000 K. For cooler stars, molecular chemistry is likely to be important, rendering the ONTARIO code invalid. We interpolate between the ZAMS models in Table 15.14 in Allen’s Astrophysical Quantities (Cox 2000) to obtain the stellar luminosities and sizes.

4.2.1. Gas and dust densities

We show the integrated luminosities from the C II 157.7 μ m and the O I 63.2 μ m lines as functions of gas peak density and dust mass in Figs. 6 & 7, respectively. In systems with little dust, gas is primarily heated through photoionization, so the C II luminosity scales almost linearly with the amount of gas. As more dust is added, photoelectric heating takes over and the C II flux starts to increase with both dust and gas density

TABLE 8
FIDUCIAL CASE DOMINANT EMISSION LINES

Species	$\lambda_{\text{vacuum}}^a$	Luminosity L_{\odot}	Flux at 20 pc $[\text{erg s}^{-1} \text{cm}^{-2}]$
C I	9826.8 Å	1.5×10^{-8}	1.2×10^{-15}
C I	9853.0 Å	4.4×10^{-8}	3.5×10^{-15}
C II	157.7 μm	2.3×10^{-8}	1.8×10^{-15}
O I	63.2 μm	1.5×10^{-10}	1.2×10^{-17}
Na I	5897.6 Å	7.6×10^{-8}	6.1×10^{-15}
Na I	5891.6 Å	1.5×10^{-7}	1.2×10^{-14}
Al I	3945.1 Å	2.2×10^{-10}	1.8×10^{-17}
Al I	3962.6 Å	4.4×10^{-10}	3.5×10^{-17}
Si II	34.8 μm	3.2×10^{-9}	2.6×10^{-16}
S I	25.2 μm	2.4×10^{-10}	1.9×10^{-17}
Ca II *	3934.8 Å	9.4×10^{-6}	7.6×10^{-13}
Ca II *	3969.6 Å	7.0×10^{-6}	5.6×10^{-13}
Ca II	7293.5 Å	3.4×10^{-7}	2.8×10^{-14}
Ca II	7325.9 Å	3.2×10^{-7}	2.5×10^{-14}
Ti II	4534.5 Å	4.2×10^{-10}	3.4×10^{-17}
Ti II	4983.1 Å	4.6×10^{-10}	3.7×10^{-17}
Ti II	3350.4 Å	1.6×10^{-7}	1.3×10^{-14}
Ti II	3362.2 Å	1.1×10^{-7}	8.8×10^{-15}
Ti II	3373.8 Å	1.1×10^{-7}	8.8×10^{-15}
Ti II	3384.7 Å	8.4×10^{-8}	6.8×10^{-15}
Cr II	8002.3 Å	7.4×10^{-8}	5.9×10^{-15}
Cr II	8127.5 Å	5.8×10^{-8}	4.7×10^{-15}
Cr II	8231.9 Å	4.7×10^{-8}	3.8×10^{-15}
Mn I	4034.2 Å	2.2×10^{-9}	1.8×10^{-16}
Mn I	4031.9 Å	3.0×10^{-9}	2.4×10^{-16}
Mn II	3443.0 Å	3.5×10^{-8}	2.8×10^{-15}
Mn II	3461.3 Å	1.8×10^{-8}	1.5×10^{-15}
Fe I	3721.0 Å	1.4×10^{-7}	1.1×10^{-14}
Fe I	3735.9 Å	8.6×10^{-8}	6.9×10^{-14}
Fe I	3821.5 Å	9.9×10^{-8}	7.9×10^{-15}
Fe I	3861.0 Å	1.3×10^{-7}	1.1×10^{-14}
Fe II	12570.9 Å	1.6×10^{-7}	1.3×10^{-14}
Fe II	13209.9 Å	4.3×10^{-8}	3.5×10^{-15}
Fe II	16440.0 Å	4.1×10^{-8}	3.3×10^{-15}
Fe II	25.99 μm	6.1×10^{-8}	4.9×10^{-15}
Ni II	6668.6 Å	1.9×10^{-8}	1.5×10^{-15}
Ni II	7379.9 Å	8.0×10^{-8}	6.4×10^{-15}
Ni II	7413.7 Å	3.1×10^{-8}	2.5×10^{-15}

NOTE. — The two Ca II lines indicated by (*) are optically thick. While our code includes the scattering of stellar flux from the star to the computational bin, it does not account for the scattering of gas emissions along the line of sight of the observer. Therefore, the computed values may significantly overestimate the luminosities in the 2 saturated calcium lines.

^aOnly lines with $\lambda \geq 3300$ Å are presented.

TABLE 9
PARAMETRIC SURVEY: OVERVIEW OF SAMPLED PARAMETERS

Parameter sampled	Min	Max	# of bins
Gas peak density	$2.4 \times 10^{-1} \text{cm}^{-3}$	$2.7 \times 10^3 \text{cm}^{-3}$	9
(total gas mass)	$(2.1 \times 10^{-6} M_{\oplus})$	$(3.3 \times 10^{-2} M_{\oplus})$	
Dust mass	$10^{-3} M_{\oplus}$	$3 M_{\oplus}$	8
Gas peak location	30 AU	190 AU	33
Gas FWHM	5 AU	95 AU	19
Gas scale height	0.05	0.95	19
Dust peak location	30 AU	190 AU	33
Dust FWHM	5 AU	95 AU	19
Dust scale height	0.05	0.95	19
Spectral types (T_{eff})	6 500 K	10 000 K	8
Elemental abundances	solar	20× solar	

(eq. [23]). For very massive dust disks, gas temperature is so high that the C II flux becomes saturated and once

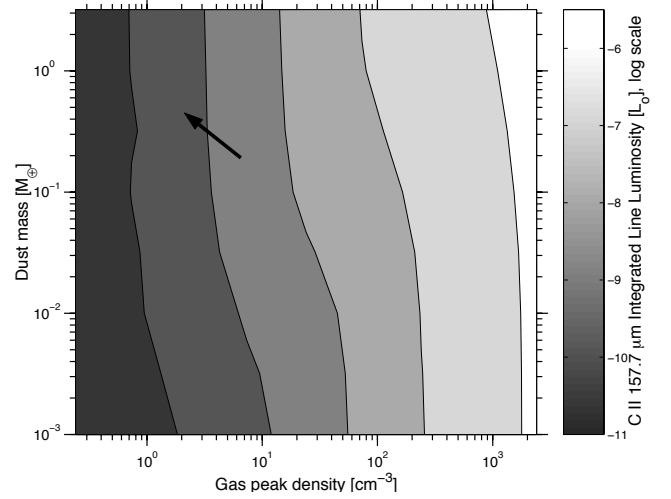


FIG. 6.— C II 157.7 μm integrated line luminosity as a function of peak gas density and total dust mass. Contours are separated by a factor of 10. The arrow shows the direction of increasing temperature.

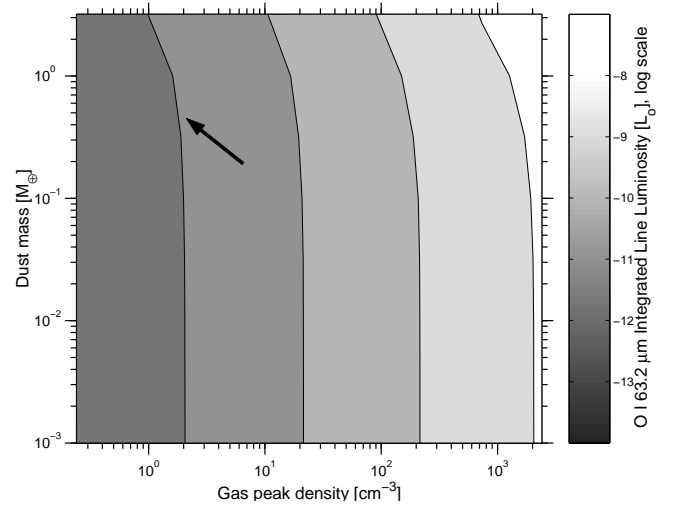


FIG. 7.— O I 63.2 μm integrated line luminosity as a function of peak gas density and total dust mass. A 10-level O I atom is used in the computation. The line luminosity is largely independent of dust mass and scales roughly linearly with gas density.

again loses its dependence on the dust mass. Despite minor features, one can summarize the results in Fig. 6 as that the C II flux rises roughly linearly with gas density.

Except for the most massive dust disks where SE begins to be dominated by the strong dust IR field, the contours for the O I 63.2 μm line flux appear independent of the dust mass for most of our disks (Fig. 7). This is explained by the fact that the line flux is almost completely dominated by radiative pumping, which masks any features from the collisional processes. To remove this masking we repeat the computation but with the O I atom having only the three lowest energy states (as opposed to the 10 levels in our normal calculation). Data both with and without the dust IR field are presented in Figs. 8 and 9, respectively. With radiative pumping disabled, the results show similar dust mass dependence

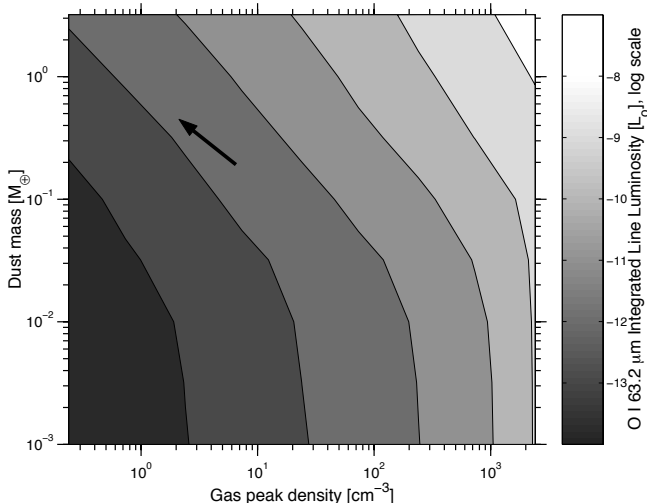


FIG. 8.— Similar to Fig. 7 except that here a 3-level O I atom is adopted. This removes the possibility of radiative pumping. Line luminosities are much weaker and they depend on dust mass.

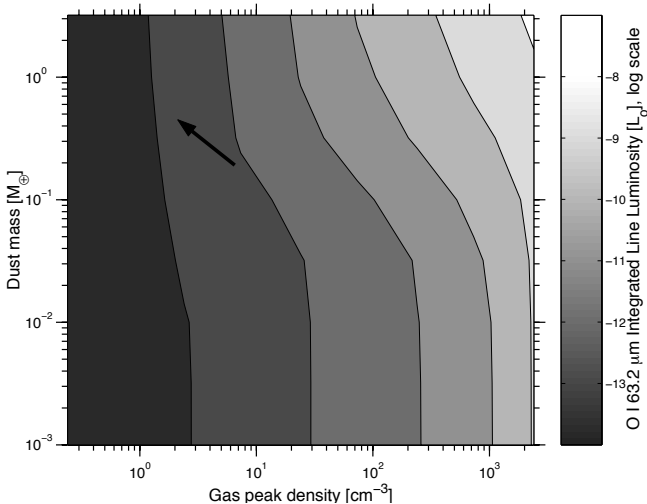


FIG. 9.— Similar to Fig. 7 except that here a 3-level O I atom is adopted, and dust IR field is disabled.

as that of the C II line. For more massive disks the flux from the cooling lines is dominated by the population equilibrium determined by the dust IR field.

In Fig. 10, cooling luminosities are presented as a function of a number of parameters that define the geometry of the gas and dust distributions.

Overall, the C II 157.7 μm luminosity is at the greatest when peaks of the gas and dust distributions coincide, allowing for maximum photoelectric heating, or when bulk of the gas is located close to the star, allowing for maximum radiative pumping and photoionization heating. The O I luminosity steadily increases as the gas distribution is moved closer to the star as this line is dominated by radiative pumping. In contrast, the radial width and the vertical scale height for the distributions do not affect line luminosities appreciably. Besides having a minimal upregulating effect on the O I 63.2 μm line flux (as observed for the β Pic configuration), changes in the dust

IR field due to varying dust profiles has no effect on the cooling line fluxes.

4.2.2. Elemental abundances

Since carbon is the dominant electron donor in the fiducial disk, increasing the carbon abundance increases n_e . This, in turn, enhances the photoelectric heating as is demonstrated by eq. [5]. The effects on the line fluxes are seen in Fig. 11 (and Table 10). In contrast, increasing the O abundance has no significant effect on the thermal balance, besides from raising the O I 63.2 μm flux by providing more atoms to be radiatively pumped.

We assume the gas to be poor in hydrogen. Raising the hydrogen abundance to its solar value increases the gas-grain collisions which cools the gas. This lowers the equilibrium gas temperature and slightly increases the photoelectric heating (and the corresponding C II cooling flux). But the effect is not significant. In fact, one can remove all elements from the gas except for C, O, Si without causing much change in the cooling line luminosities (Table 10).

TABLE 10
LINE LUMINOSITIES AS FUNCTIONS OF ELEMENTAL ABUNDANCES

Modification ^a	C II 157.7 μm	O I 63.2 μm
	[L_\odot]	[L_\odot]
Fiducial	2.3×10^{-8}	1.3×10^{-10}
$n_C = n_{C,\odot}$	3.8×10^{-10}	1.2×10^{-10}
$n_O = 20 n_{O,\odot}$	2.3×10^{-8}	2.5×10^{-9}
$n_H = n_{H,\odot}$	2.6×10^{-8}	1.3×10^{-10}
C, O, Si only ^b	2.3×10^{-8}	1.3×10^{-10}

^aFiducial case inputs are used except for the parameter mentioned.

^bAll elements except for C, O, Si and H are removed.

4.2.3. Stellar spectral type

In Fig. 12, C II 157.7 μm , O I 63.2 μm and 145.5 μm luminosities are plotted against stellar spectral types (represented by their respective effective temperatures). The C II 157.7 μm line remains dominant for all spectral types. Its luminosity is constant for $T_{\text{eff}} \leq 8000$ K. Around more luminous stars the excited level of C II is populated mostly by stellar radiation (through fluorescence of UV lines), rather than by collisions with electrons. In this regime, the C II 157.7 μm flux is greater than the actual cooling and it increases with T_{eff} until T_{eff} reaches ~ 10000 K. Relatedly, level population in the excited states of the O I atoms is dominated by radiative pumping for all stars with $T_{\text{eff}} \geq 7500$ K. As a result, the line flux rises with T_{eff} above 7500 K.

5. CONCLUSIONS

We have produced a thermal and statistical equilibrium code to specifically address gas emission from dusty gas-poor disks around A–F stars, motivated by the recent launch of the far-infrared observatory *Herschel*, as well as the discovery of gas in a number of debris disk systems. We study the effects of, among other things, photoelectric heating from dust grains, photoionization heating of the gas, thermal equilibrium reached in the disk, statistical equilibrium of atoms in the disk, and cooling by

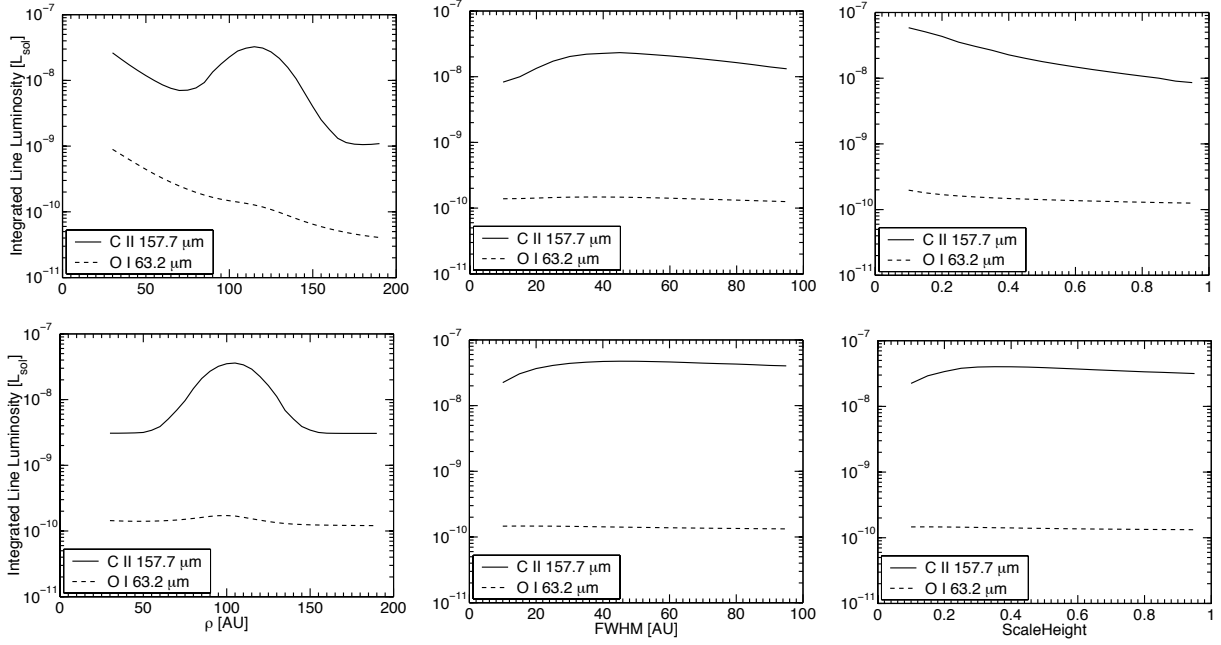


FIG. 10.— C II 157.7 μm and O I 63.2 μm integrated line luminosities as functions of gas (top) and dust (bottom) peak cylindrical radii (left panels), their radial FWHM (middle panels) and their scale heights (right panels). One parameter is varied at a time. Only the left panels show strong dependence – the line radiation is enhanced whenever the peak radii for the dust and the gas coincide, or when bulk of the gas lies very close to the star.

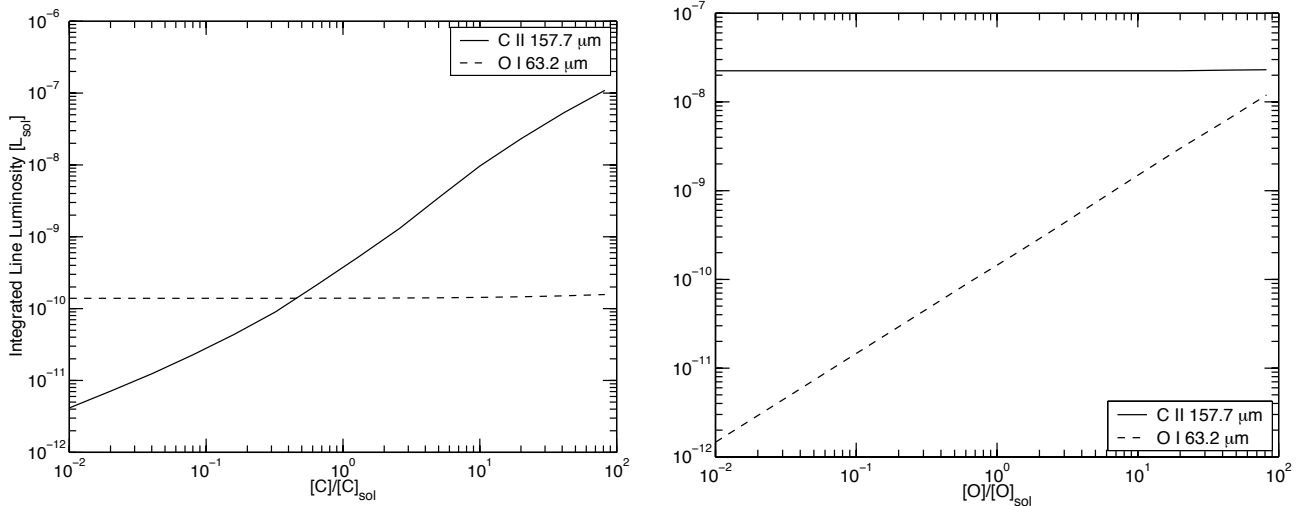


FIG. 11.— C II 157.7 μm and O I 63.2 μm integrated line luminosities as function of C (left) and O (right) abundances. The former rises with carbon abundance, while the latter with oxygen abundance, but the reasons behind are somewhat different (see text).

infrared atomic lines. Details about the code (ONTARIO) are presented in the appendix.

Using this code and disk parameters that resemble the observed β Pic gas disk, we have computed a range of observables, including the line luminosities from infrared transitions, the emission and absorption of optical and UV lines, and the column densities of metals in the disk.

As a guidance for observations to be carried out on Herschel and other telescopes, we explore the dependence of the infrared line luminosities on disk parameters. Our findings are summarized below:

- for most of the configurations surveyed, we find that the C II 157.7 μm line is the most luminous. The expected flux for the β Pic disk is $\sim 10^{-14}$ $\text{erg s}^{-1} \text{cm}^{-2}$, which should be easily detectable by *Herschel*.
- the O I lines, initially thought to be important cooling lines (Besla & Wu 2007), have underwhelming luminosities due to NLTE effects. Most of the luminosities in these lines arise from fluorescence of stellar UV photons, as opposed to from collisional cooling of the gas. The flux from the O I 63.2 μm

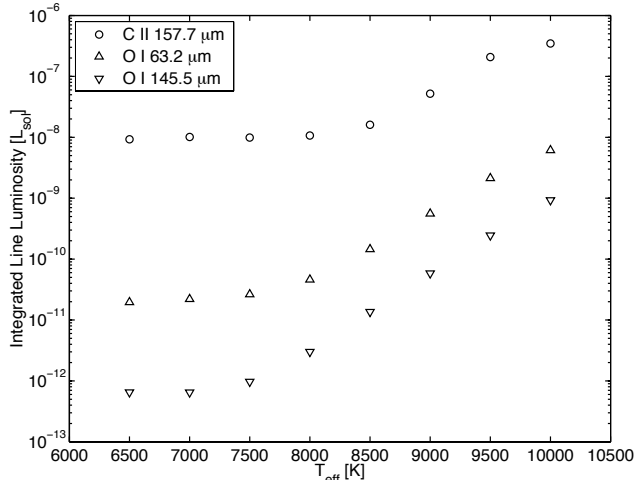


FIG. 12.— C II 157.7 μm and O I 63.2 μm , 145.5 μm integrated line luminosities as function of effective temperature (T_{eff}) of the central main-sequence star. Around stars with $T_{\text{eff}} \gtrsim 8500$ K, the level population of C II is dominated by radiative pumping, while population in O I is dominated by radiative pumping for stars with $T_{\text{eff}} \gtrsim 7500$ K.

line will be too faint to reasonably be detected by *Herschel*.

- over the parameter range we sample, the C II line flux scales roughly linearly with the gas density, with the carbon elemental abundance, and rises with the effective temperature of the star. Line

fluxes also reach maximum when the dust and gas components in the disk align radially.

We note two major caveats in our model:

- in some of our models, the gas temperature rise above 5000 K. This is possibly an artificial result because we have not included all relevant gas cooling mechanisms. We have performed preliminary tests by considering other fine transition lines listed in (Hollenbach & McKee 1989) but do not find them of importance. However, if this high temperature feature does occur in real disks, it implies loss of metallic gas by thermal evaporation.
- we have assumed that molecular species are unimportant for the thermal equilibrium of the gas. For cooler stars, a significant amount of the gas may be in molecular phases (CH, CO,...) and this may impact our predictions of infrared line luminosities.

By comparing ONTARIO predictions with observations, one may hope to infer physical properties of the debris disks, including gas density and elemental abundances. With the new observing windows being opened up by *Herschel*, *SOFIA*, and *ALMA*, we expect many new observational results that will require interpretation by models such as ONTARIO.

KZ was funded under NSERC USRA scholarship. AB is funded by the *Swedish National Space Board* (contract 84/08:1), and YW acknowledges the NSERC support. We thank the referee Inga Kamp for many detailed and insightful comments, which helped improve the manuscript.

APPENDIX THE ONTARIO CODE

An overview of ONTARIO’s program flow is shown in Fig. 13. ONTARIO in principle consists of a master routine and four principal subroutines. The four subroutines are:

1. *Geometry solver*: defines the geometry and produces observables from the solution. Our models are currently two dimensional (radius and height), but could in principle be of any geometry. The geometry solver computes the projected flux from the defined geometry.
2. *Ionization balance*: given a temperature, radiation field, and elemental abundances, it guesses an electron density and then iterates until the derived electron density (computed from the ionization of the actual elements input) agrees with the assumed electron density. Ionization cross-sections and recombination coefficients are retrieved from the CLOUDY code (Ferland 2005), and are restricted to the first 30 elements (atomic numbers 1–30, hydrogen through zinc). To estimate the radiation field, we use NextGen stellar atmospheres (Hauschildt et al. 1999) with solar abundance and main sequence surface $\log g$. No chromosphere emission is estimated in general, but the interstellar radiation field (from Weingartner & Draine 2001) and cosmic ray ionization ($2 \times 10^{-17} \text{ s}^{-1} \text{ atom}^{-1}$, from Spitzer 1978) are included.
3. *Thermal balance*: given an ionization state, dust density and radiation field, this routine computes all relevant heating and cooling mechanisms (as outlined in §2) assuming an initial temperature, and then modifying the assumed temperature until the heating equals the cooling. If the resulting temperature is different from what was assumed for the ionization balance, that routine recomputes the ionization state, which is then input to the thermal balance routine for a new thermal balance computation.
4. *Level population*: given a radiation field, an electron density and electron temperature, the electronic energy level population is calculated using a statistical equilibrium (SE) of all considered transitions for given elements. This routine is mostly used at the end, when the physical state of the disk is already computed, as most levels and species do not participate in the cooling of the disk. The exception is O I, C II, and Si II where we do include a

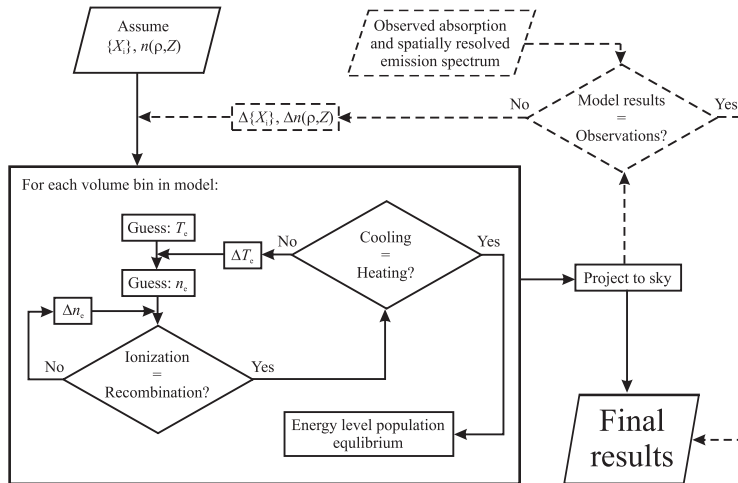


FIG. 13.— Model flowchart describing the ONTARIO code. The dashed path illustrates how the code is run when fitting observations.

statistical equilibrium computation already in the thermal balance computation, because of the important cooling lines of those species. The radiative data for all atomic species was taken from the NIST Atomic Spectra Database (Ralchenko 2005) and the Kurucz Atomic Spectral Line Database (Kurucz 1995). The transition data from the two sources were combined to produce a more complete energy level set. Collisional coefficients for the cooling C II and O I lines were obtained from the Iron Project (Pradhan 2000) and Silva & Viegas (2001), respectively; for C I, Si I, Si II and S I from Hollenbach & McKee (1989). Collisional data for other electron transition lines were taken from the Iron Project (Pradhan 2000) for C II, Ni II, Fe I, Fe II. At higher temperatures, where there were no data available, the collisional strength was extrapolated using a first order polynomial fit in the log-log space. The number of levels and transitions for different elements included in ONTARIO are summarized in Table 11.

ONTARIO assumes the disk is optically thin in the continuum, so that simplified radiative transfer can be used for both the ionization and thermal balance, which simplifies the computation greatly and allows for more general geometries (compared to, e.g., CLOUDY).

Collisional strengths γ for the electronic transition lines for the majority of atomic species are not available from literature. γ is calculated by taking into account a number of quantum effects (see, for example, Zhang & Pradhan (1995)) and no simple relationship exists between the collisional strengths and the energy associated with a transition line. Since we were only able to obtain collisional data for the Si II fine structure cooling line and not other higher level electronic transitions, we investigated whether this might result in incorrect determination of the gas temperature. Results of running the code with and without C II non-cooling collisional strengths (that is, setting $q_{ij} = q_{ji} = 0$ for $i, j \neq 1, 0$) for a number of bins produced no noticeable change in the computed temperatures (within 1 K). Therefore, all non-cooling electron transitions can be treated as purely radiative for gas densities representative of debris disks.

SE calculation is the most computationally expensive part of the numerical model. An example on the extreme side is Fe II, which has 790 electron energy levels and 54054 transitions. To solve SE for this atomic species matrix of 54054 elements has to be inverted for each bin in the grid (the actual number of levels used was reduced to 300 lower levels: the population of the higher levels is negligible, and this reduction significantly improved computation time). Furthermore, while O I, C II and Si II have substantially less electron energy levels (150, 191 and 143 respectively) and corresponding transitions (1048, 1347 and 927 respectively), SE for these species participating in cooling of the gas has to be solved multiple times for each bin when recursively computing thermal equilibrium.

To avoid a full SE computation, 2 and 3-level atom approximation for C II and O I fine structure line cooling, respectively, were previously used in similar simulations (Hollenbach & McKee 1989; Kamp & van Zadelhoff 2001). We used ONTARIO to test the validity of this assumption for the hotter stars sampled by our model. For C II around a $T_{\text{eff}} = 10000$ K star we found a factor of 4 increase in the cooling line flux when using an ion with all the energy levels compared to a 2-level approximation. The difference was determined to be due to fluorescence (radiative pumping to higher levels). While the $0 \rightarrow 1$ energy transition is radiatively forbidden, ground state electrons can get photo-excited to higher energy levels and then spontaneously decay to the first excited level. Our results show that a 2-level C II approximation underestimates the population of level 1, and consequently the $1 \rightarrow 0$ emission flux. The effect is more pronounced closer to the star where the photo-excitation is more important. Similar results were seen for O I and Si II. Furthermore, since gas densities are substantially below $n_{e,\text{crit}}$ for these species, the effect of radiative pumping is much stronger. In fact, using a significantly reduced number of levels for O I and Si II can for some system configurations underestimate flux by more than a factor of a 100. In addition, strong radiative pumping can overpopulate the first excited energy state beyond its LTE level, leading to stronger collisional de-excitation than excitation flux. In this regime the fine-structure transition becomes a heating line, injecting stellar energy into the gas. This effect is absent when radiative transitions are excluded.

We further tested the effect of reducing the number of energy levels for the cooling atoms and determined that a limited reduction did not significantly effect the computed temperature and line fluxes. Using 10 level approximations for C II, Si II and O I species kept temperature close to the full-level species results and produced similar line fluxes. However, the decrease in computation time was significant. For example, reducing C II from 191 to 10 energy levels decreases execution time by a factor of ~ 365 (the square of the level reduction). Therefore, we used these limited reduction cooling species approximations in all further numerical runs.

TABLE 11
NUMBER OF ENERGY LEVELS AND TRANSITIONS INCLUDED IN ONTARIO

Species	# of Energy Levels	# of Transitions	Refs for collisional rates.
C I	611	7597	Hollenbach & McKee (1989)
C II	191	1347	Pradhan (2000)
O I	150	1048	Silva & Viegas (2001)
Na I	58	452	...
Mg II	57	540	...
Al I	213	798	...
Al II	153	2167	...
Si I	598	6557	Hollenbach & McKee (1989)
Si II	143	927	Hollenbach & McKee (1989)
S I	114	720	Hollenbach & McKee (1989)
Ca II	67	625	...
Ti I	394	12709	...
Ti II	213	4571	...
Cr II	725	36350	...
Mn I	431	9451	...
Mn II	503	18950	...
Fe I	497	18349	Pradhan (2000)
Fe II	300	13992	Pradhan (2000)
Ni II	682	30767	Pradhan (2000)
Zn I	35	1135	...
Zn II	6	6	...

NOTE. — The radiative data for all atomic species was taken from the NIST Atomic Spectra Database (Ralchenko 2005) and the Kurucz Atomic Spectral Line Database (Kurucz 1995). No collisional data were available for Na I, Mg II, Al I, Al II, Ca II, Ti I, Ti II, Cr II, Mn I, Mn II, Zn I and Zn II.

NOTE. —

REFERENCES

- Besla, G. & Wu, Y. 2007, *ApJ*, 655, 528
 Beust, H. & Valiron, P. 2007, *A&A*, 466, 201
 Brandeker, A., Liseau, R., Olofsson, G., & Fridlund, M. 2004, *A&A*, 413, 681
 Chen, C. H. & Jura, M. 2003, *ApJ*, 582, 443
 Chen, C. H., Li, A., Bohac, C., Kim, K. H., Watson, D. M., van Cleve, J., Houck, J., Stapelfeldt, K., Werner, M. W., Rieke, G., Su, K., Marengo, M., Backman, D., Beichman, C., & Fazio, G. 2007, *ApJ*, 666, 466
 Chen, C. H., Sargent, B. A., Bohac, C., Kim, K. H., Leibensperger, E., Jura, M., Najita, J., Forrest, W. J., Watson, D. M., Sloan, G. C., & Keller, L. D. 2006, *ApJS*, 166, 351
 Cox, A. N. 2000, *Allen's astrophysical quantities* (Allen's Astrophysical Quantities)
 Crawford, I. A., Beust, H., & Lagrange, A.-M. 1998, *MNRAS*, 294, L31
 Czechowski, A. & Mann, I. 2007, *ApJ*, 660, 1541
 Dominik, C. & Decin, G. 2003, *ApJ*, 598, 626
 Draine, B. T. 1978, *ApJS*, 36, 595
 —. 2003, *ApJ*, 598, 1017
 Ferland, G. J. 2005, in *Bulletin of the American Astronomical Society*, 477–+
 Fernández, R., Brandeker, A., & Wu, Y. 2006, *ApJ*, 643, 509
 Gorti, U. & Hollenbach, D. 2004, *ApJ*, 613, 424
 —. 2009, *ApJ*, 690, 1539
 Grevesse, N. & Noels, A. 1993, in *Origin and Evolution of the Elements*, ed. N. Prantzos, E. Vangioni-Flam, & M. Casse, 14–+
 Haisch, Jr., K. E., Lada, E. A., & Lada, C. J. 2001, *ApJ*, 553, L153
 Hauschildt, P. H., Allard, F., & Baron, E. 1999, *ApJ*, 512, 377
 Heap, S. R., Lindler, D. J., Lanz, T. M., Cornett, R. H., Hubeny, I., Maran, S. P., & Woodgate, B. 2000, *ApJ*, 539, 435
 Herczeg, G. J., Linsky, J. L., Walter, F. M., Gahm, G. F., & Johns-Krull, C. M. 2006, *ApJS*, 165, 256
 Hobbs, L. M., Vidal-Madjar, A., Ferlet, R., Albert, C. E., & Gry, C. 1985, *ApJ*, 293, L29
 Holland, W. S., Greaves, J. S., Zuckerman, B., Webb, R. A., McCarthy, C., Coulson, I. M., Walther, D. M., Dent, W. R. F., Gear, W. K., & Robson, I. 1998, *Nature*, 392, 788
 Hollenbach, D. & McKee, C. F. 1989, *ApJ*, 342, 306
 Ida, S. & Lin, D. N. C. 2004, *ApJ*, 616, 567
 Jayawardhana, R., Coffey, J., Scholz, A., Brandeker, A., & van Kerkwijk, M. H. 2006, *ApJ*, 648, 1206
 Jonkheid, B., Kamp, I., Augereau, J.-C., & van Dishoeck, E. F. 2006, *A&A*, 453, 163
 Kamp, I. & Bertoldi, F. 2000, *A&A*, 353, 276
 Kamp, I. & van Zadelhoff, G.-J. 2001, *A&A*, 373, 641
 Kamp, I., van Zadelhoff, G.-J., van Dishoeck, E. F., & Stark, R. 2003, *A&A*, 397, 1129
 Klahr, H. & Lin, D. N. C. 2005, *ApJ*, 632, 1113
 Kurucz, R. L. 1995, in *Astronomical Society of the Pacific Conference Series*, Vol. 78, *Astrophysical Applications of Powerful New Databases*, ed. S. J. Adelman & W. L. Wiese, 205–+
 Lecavelier des Etangs, A., Vidal-Madjar, A., Roberge, A., Feldman, P. D., Deleuil, M., André, M., Blair, W. P., Bouret, J.-C., Désert, J.-M., Ferlet, R., Friedman, S., Hébrard, G., Lemoine, M., & Moos, H. W. 2001, *Nature*, 412, 706
 Lovelace, R. V. E., Romanova, M. M., & Barnard, A. W. 2008, *MNRAS*, 389, 1233
 Lynden-Bell, D. & Pringle, J. E. 1974, *MNRAS*, 168, 603
 Najita, J., Carr, J. S., & Mathieu, R. D. 2003, *ApJ*, 589, 931

- Nilsson, R., Liseau, R., Brandeker, A., Olofsson, G., Risacher, C., Fridlund, M., & Pilbratt, G. 2009, *A&A*, 508, 1057
- Olofsson, G., Liseau, R., & Brandeker, A. 2001, *ApJ*, 563, L77
- Osterbrock, D. E. 1989, *Astrophysics of gaseous nebulae and active galactic nuclei* (Research supported by the University of California, John Simon Guggenheim Memorial Foundation, University of Minnesota, et al. Mill Valley, CA, University Science Books, 1989, 422 p.)
- Pascucci, I., Gorti, U., Hollenbach, D., Najita, J., Meyer, M. R., Carpenter, J. M., Hillenbrand, L. A., Herczeg, G. J., Padgett, D. L., Mamajek, E. E., Silverstone, M. D., Schlingman, W. M., Kim, J. S., Stobie, E. B., Bouwman, J., Wolf, S., Rodmann, J., Hines, D. C., Lunine, J., & Malhotra, R. 2006, *ApJ*, 651, 1177
- Pradhan, A. K. 2000, in *Atomic Data Needs for X-ray Astronomy*, p. 69, ed. M. A. Bautista, T. R. Kallman, & A. K. Pradhan, 69–+
- Ralchenko, Y. 2005, *Memorie della Societa Astronomica Italiana Supplement*, 8, 96
- Redfield, S. 2007, *ApJ*, 656, L97
- Redfield, S., Kessler-Silacci, J. E., & Cieza, L. A. 2007, *ApJ*, 661, 944
- Rieke, G. H., Su, K. Y. L., Stansberry, J. A., Trilling, D., Bryden, G., Muzerolle, J., White, B., Gorlova, N., Young, E. T., Beichman, C. A., Stapelfeldt, K. R., & Hines, D. C. 2005, *ApJ*, 620, 1010
- Roberge, A., Feldman, P. D., Lagrange, A. M., Vidal-Madjar, A., Ferlet, R., Jolly, A., Lemaire, J. L., & Rostas, F. 2000, *ApJ*, 538, 904
- Roberge, A., Feldman, P. D., Weinberger, A. J., Deleuil, M., & Bouret, J.-C. 2006, *Nature*, 441, 724
- Roberge, A. & Weinberger, A. J. 2008, *ApJ*, 676, 509
- Roberge, A., Weinberger, A. J., Redfield, S., & Feldman, P. D. 2005, *ApJ*, 626, L105
- Silva, A. I. & Viegas, S. M. 2001, *Computer Physics Communications*, 136, 319
- Slettebak, A. 1975, *ApJ*, 197, 137
- Spangler, C., Sargent, A. I., Silverstone, M. D., Becklin, E. E., & Zuckerman, B. 2001, *ApJ*, 555, 932
- Spitzer, L. 1978, *Physical processes in the interstellar medium*
- Thi, W. F., Blake, G. A., van Dishoeck, E. F., van Zadelhoff, G. J., Horn, J. M. M., Becklin, E. E., Mannings, V., Sargent, A. I., van den Ancker, M. E., & Natta, A. 2001, *Nature*, 409, 60
- Weingartner, J. C. & Draine, B. T. 2001, *ApJS*, 134, 263
- Wyatt, M. C., Smith, R., Su, K. Y. L., Rieke, G. H., Greaves, J. S., Beichman, C. A., & Bryden, G. 2007, *ApJ*, 663, 365
- Zhang, H. L. & Pradhan, A. K. 1995, *A&A*, 293, 953
- Zuckerman, B., Forveille, T., & Kastner, J. H. 1995, *Nature*, 373, 494